



HAL
open science

A search for life in Palaeoproterozoic marine sediments using Zn isotopes and geochemistry

Abderrazak El Albani, K.O. Konhauser, A. Somogyi, J. Ngwalghoubou Ikouanga, A. Lamboux, J. Blichert-Toft, E. Chi-Fru, C. Fontaine, A. Mazurier, A. Riboulleau, et al.

► To cite this version:

Abderrazak El Albani, K.O. Konhauser, A. Somogyi, J. Ngwalghoubou Ikouanga, A. Lamboux, et al.. A search for life in Palaeoproterozoic marine sediments using Zn isotopes and geochemistry. *Earth and Planetary Science Letters*, 2023, 612, pp.118169. <10.1016/j.epsl.2023.118169>. <hal-04095643>

HAL Id: hal-04095643

<https://hal.science/hal-04095643v1>

Submitted on 12 May 2023

HAL is a multi-disciplinary open access archive for the deposit and dissemination of scientific research documents, whether they are published or not. The documents may come from teaching and research institutions in France or abroad, or from public or private research centers.

L'archive ouverte pluridisciplinaire HAL, est destinée au dépôt et à la diffusion de documents scientifiques de niveau recherche, publiés ou non, émanant des établissements d'enseignement et de recherche français ou étrangers, des laboratoires publics ou privés.



Distributed under a Creative Commons CC BY-NC 4.0 - Attribution - Non-commercial use - International License

A search for life in Palaeoproterozoic marine sediments using Zn isotopes and geochemistry

A. El Albani^{1*}, K.O. Konhauser², A. Somogyi³, J. Ngwalghoubou Ikouanga¹, A. Lamboux⁴, J. Blichert-Toft^{4,5}, E. Chi-Fru⁶, C. Fontaine¹, A. Mazurier¹, A. Riboulleau⁷, A.-C. Pierson-Wickmann⁸, and F. Albarède^{4,5}

¹*Institut de Chimie des Milieux et Matériaux, Université de Poitiers and CNRS, 86073 Poitiers, France.*

²*Department of Earth and Atmospheric Sciences, University of Alberta, Edmonton, AB T6G 2E3, Canada.*

³*Nanoscopium Beamline Synchrotron Soleil, BP 48, Saint-Aubin, Gif-sur-Yvette 91192, France.*

⁴*Laboratoire de Géologie de Lyon, CNRS UMR 5276, Ecole Normale Supérieure de Lyon, and Université de Lyon, 69007, Lyon, France.*

⁵*Department of Earth, Environmental and Planetary Sciences, Rice University, Houston, TX 77005, USA.*

⁶*School of Earth and Ocean Sciences, Centre for Geobiology and Geochemistry, Cardiff University, Cardiff LF10 3AT, Wales, UK.*

⁷*UMR 8187 CNRS LOG, University of Lille, ULCO, Villeneuve d'Ascq 59655, France.*

⁸*Geosciences Rennes, CNRS UMR 6118, Université de Rennes, Rennes Cedex, 35042, France.*

*Corresponding author: A. El Albani (abder.albani@univ-poitiers.fr)

Keywords: Life form; Early Proterozoic; Zinc isotopes; Eukaryotes; Prokaryotes

Abstract

Sediments from the 2.1- to 1.9-billion-year-old Francevillian Group in southeastern Gabon include centimeter-sized pyritized structures suggestive of colonial organisms (El Albani et al., 2010), some of which may have been motile (El Albani et al., 2019). However, these interpretations were largely based on morphological and geochemical characteristics that lack metabolic clues and/or can be explained by abiotic processes. To move this work forwards, we describe other centimeter-sized specimens, loosely referred to as lenticular forms (LF), from the same area and apply a more holistic approach including morphology, mineralogy, and geochemistry. The objects are 0.2–4 cm in diameter, and most of them are endowed with a regular brim that scales proportionally to external diameter reminiscent of biological order, hence rendering the LF putative biogenic traces. The LF are perfectly delineated in every direction and deflect the sedimentary layers on which they rest. X-ray microtomography further demonstrates that the LF are syn-depositional features and not

40 concretions, while lead isotope systematics indicate that the geochemical imprint of diagenesis is
41 inconsequential. Low sulfur content is largely concentrated in the organic matrix, and scarcity of
42 pyrite and its persistence as micron-sized crystals show that the role of sulfate reduction is minor.
43 Most interestingly, the fillings of the LF cavities show large and correlated excesses of organic carbon
44 and zinc, with the latter being distinctly enriched in its light isotopes. The geochemical anomalies of
45 the fillings relative to the host rock, notably those associated with Zn, clearly were buried with the
46 LF, and further imply biogenicity. In this regard, a ten-fold increase in LF size towards the top of the
47 black shale series might be related to increasing Zn (nutrient) availability. Although we cannot
48 conclude with any certainty what these remnant organisms were, their features all taken together
49 are evocative of very large agglutinate protists that grazed on bacterial biomass either in the water
50 column or as benthic mats.

51

52 **1. Introduction**

53 The composition of the Archean and Paleoproterozoic biosphere remains uncertain largely due to
54 the scarcity of an unequivocal Precambrian palaeobiological record. The recovery of benthic
55 microfossils – the physical remains of microorganisms that grew attached to ancient sediments –
56 has provided relevant guidance for understanding the trajectory of biological evolution (Butterfield,
57 2007; Knoll, 2014), but ultimately their interpretation is based primarily on subjective morphological
58 features. The difficulties associated with such determinations are well-identified and repeatedly
59 reviewed (see a recent account with references in Neveu et al., 2018). In short, abiotic processes
60 can almost always explain features reminiscent of microfossils. Moreover, demonstrating the
61 biological nature of putative fossil remains in ancient terrestrial rocks is a formidable challenge due
62 to post-depositional alteration via burial, lithification, and secondary fluid flow through porous and
63 fractured rocks (Neveu et al., 2018).

64

65 Spectroscopy and geochemistry offer another approach. Vibrational, infrared, and Raman
66 spectroscopy, for example, allows the molecular compounds present in organic material and the
67 thermal maturity of a fossil to be determined (Hickman-Lewis et al., 2016; Olcott Marshall and
68 Marshall, 2015). Carbon isotope analysis (Rosing, 1999; Tashiro et al., 2017) of carbonaceous
69 remains adds a strong component to help determine the biogenic character, or not, of a given relic.
70 But both techniques are sensitive to metamorphic alteration and to date have been more efficient
71 at characterizing unambiguous fossils and less at providing incontrovertible proof of the nature of
72 enigmatic biological traces (Marshall et al., 2005; Sforza et al., 2014), particularly in carbon-rich
73 materials. Trace elemental geochemistry as a tool suitable for the quest of biogenicity has also been
74 applied. Using microbeam particle-induced X-ray emission (μ PIXE), Hickman-Lewis et al. (2020)
75 demonstrated association of transition metals and metalloids with carbonaceous materials in 3.33
76 Ga-old cherts from the Barberton greenstone belt and suggested that patterns in elemental
77 abundance might help constrain the metabolic networks present in fossilized ecosystems. Gangidine
78 et al. (2021) analyzed hot-spring deposits from the mid-Paleozoic Drummond Basin, Australia, but
79 the elements for which they identified excesses associated with putative fossils would normally
80 qualify as terrigenous for modern oceanographers. Sforza et al. (2022) recently showed associations
81 of nickel with putative porphyrins in Proterozoic microfossils. Sedimentological evidence for a

82 biological role of this highly toxic and poorly chelated element in organic-rich material still remains
83 ambiguous as nickel isotope analysis suggests that isotope fractionation may be an effect of the
84 weathering environment (Porter et al., 2014). Other micro-nutrients, notably cobalt, copper, iron,
85 manganese, and molybdenum are all essential for biological activity, yet most of these elements are
86 redox-sensitive and, thus, their concentrations and isotopic signatures, whenever more than one
87 isotope is present, are readily overprinted by the decay of organic matter and diagenesis (Wacey,
88 2009).

89

90 Apart from iron, zinc is the most abundant trace element in modern plankton (Twining and Baines,
91 2013) and, therefore, is particularly useful as a potentially strong biosignature. Further, Zn^{2+} is non-
92 toxic, redox-*insensitive*, and of all the transition elements, it shows the highest affinity for a large
93 spectrum of ligands of biological interest. This makes Zn a versatile element in thousands of proteins
94 of biological interest, in particular as a co-factor of carbonic anhydrase, alkaline phosphatase, zinc
95 fingers, and other biological components (Weber et al., 2018). Zinc is known to be protective against
96 oxidative and saline stress as well as increasing membrane stability in plants (Tufail et al., 2018).
97 Importantly, unlike carbon and nitrogen, Zn has the potential for preserving both chemical and
98 isotopic memories of biological precursors of cyanobacteria, algae, and other aquatic
99 photoautotrophs. Preferential uptake of light Zn isotopes by organic material has been clearly
100 considered by earlier Zn isotope work on modern carbonates (Pichat et al., 2003) and on the water
101 column (Weber et al., 2018), but has not so far been explicitly considered as a useful biogenicity
102 indicator. This is the purpose of the present work, which makes a strong case in favor of Zn
103 abundances and isotopic compositions as a new biosignature.

104

105 Contrary to complex and potentially misleading morphological criteria, with well-known cases being
106 the ALH84001 Martian meteorite (Neveu et al., 2018), ‘cyanobacterial filaments’ in the 3465 Ma
107 Apex Chert in the Pilbara Craton, Western Australia (Brasier et al., 2002), and the purported
108 stromatolites from the 3.7 Ga old Isua supracrustal belt, southwest Greenland (Allwood et al., 2018),
109 well-resolved spectroscopic and geochemical measurements are repeatable by any observer or
110 analyst with a reproducible outcome. Here we will focus primarily on the geochemical approach and
111 test whether, among other geochemical tracers, Zn and its isotopes may help track ancient life on
112 early Earth and other planets.

113

114 Specifically we address the issue of biogenicity in deep-time sedimentary rocks by using a particular
115 group of putative biological traces found in sediments from the Francevillian series deposited in the
116 2.1 to 1.9 Gy interval, previously described in a series of publications (El Albani et al., 2010; El Albani
117 et al., 2014; El Albani et al., 2019) and referred to here as lenticular forms (LF). The decisive
118 advantages of the Gabon putative life forms over those from the Late Proterozoic and the Cambrian,
119 such as the Burgess Shale (Butterfield et al., 2007; Gaines et al., 2019; Powell, 2003), is their very
120 mild degree of diagenesis; their huge enrichment in organic carbon (up to 10%) and bitumen, and
121 their deposition in an oxygen-poor, clay-rich environment that offers a higher degree of
122 preservation potential. We combine macroscopic and tomographic morphological evidence with a

123 broad coverage of major and trace element and isotopic evidence, with emphasis on Zn, to address
124 hotly debated questions that generally accompany ancient putative traces of life:

125

- 126 a) Could biological-like morphology be an artefact of early or late diagenesis or even be
127 concretions?
128 b) What is the chemical imprint of diagenesis and in particular the role of sulfate reduction?
129 c) If the enigmatic investigated traces are of biogenic origin, which order do they represent,
130 typically prokaryotes vs eukaryotes, multicellular colonial vs metazoan organisms?

131

132 In addition to the issue of biogenicity, the present work is relevant to two other broad questions
133 pertinent to early life reconstruction. First, could the emergence of eukaryotes, largely believed to
134 have taken place at the onset of the Mesoproterozoic ~1.6 Gy ago, instead have arisen much earlier
135 (Javaux and Lepot, 2018; Knoll, 2014)? Second, what is the relevance of the putative Gabon life
136 forms to the ~2.1 Ga old Lomagundi event, a period characterized by the burial of organic matter
137 and increased atmospheric oxygenation (Melezhik et al., 2013; Canfield et al., 2013; Mänd et al.,
138 2020).

139 **2. Geological and sedimentary setting**

140 The Francevillian basin consists of 35,000 km² of unmetamorphosed sedimentary rocks that were
141 deposited on the margin of the Birimian (Eburnean) craton during the Paleoproterozoic Eon in an
142 epicontinental setting in what is now the Republic of Gabon, western equatorial Africa (Bonhomme
143 et al., 1982; Bros et al., 1992; Reynaud et al., 2018) (Fig. 1). The sediment package is between 1000
144 and 2500 m thick and is subdivided into four lithostratigraphic units, FA to FD, which rest
145 unconformably on Archean basement rocks. The FA unit mainly consists of fluvial and deltaic
146 sandstones. At the top, it contains uranium enrichments and hosts the well-known Oklo natural
147 nuclear reactors (Gauthier-Lafaye et al., 1989). These reactors are heat sources that trigger the
148 convection of interstitial fluids. The FB unit consists of marine sediments deposited mainly below
149 the storm wave base. It has been recognized as the source of massive petroleum generation which
150 played a major role in the formation of the uranium-rich deposits that triggered the Oklo natural
151 nuclear reactors (Mossman, 2001). Because of its diverse lithological composition, the FB unit is
152 further divided into the FB1 (a, b, and c) and FB2 (a and b) subunits. The FB1a and FB1b subunits
153 consist of interlayered shales, sandstones, and conglomerates, fining upwards to predominantly
154 shales at the top. The FB1c subunit consists of shales, but also contains a thin iron formation overlain
155 by black shales and a thick interval rich in manganese. The FB2a subunit consists of sandstone beds
156 deposited in channels near the fair-weather wave base. These are sharply overlain by the FB2b
157 subunit including finely-laminated black shales (Fig. 2) interbedded with thin siltstone layers
158 deposited by waning storm surges. All of the specimens presented here were collected from the
159 FB2b black shales (Fig. 2). In the quarry that was investigated, the FB2b black shales are 5 m thick.
160 The overlying FC unit is dominated by dolomites and stromatolitic cherts, indicating shallow-water
161 conditions. The FD unit corresponds to black shales deposited during a transgressive phase. A large
162 portion of the Francevillian series was deposited during the Lomagundi-Jatuli Event carbon isotope
163 excursion dated in the Transfennoscandian Greenstone Belt at ca. 2.22-2.06 Ga (Canfield et al.,
164 2013; Martin et al., 2013) but, on a global scale, they may be basin-specific or diachronous and could

165 locally extend to younger ages (Martin et al., 2015). The preservation of randomly ordered smectite-
166 rich illite/smectite mixed layer minerals (R0-type) demonstrates unusually slow mineral
167 transformation and only a moderate degree of diagenesis, which is remarkable considering the
168 Paleoproterozoic age of the sedimentary succession (Gauthier-Lafaye et al., 1996). It also has no
169 indication of hydrothermal influence (Gauthier-Lafaye et al., 1996).

170 Previous publications assessed that the Francevillian black shales were deposited from an
171 oxygenated water column in a quiet, low-energy marine environment (Canfield et al., 2013; El Albani
172 et al., 2010). They are interbedded with thin sandstone layers lacking specimens. They are
173 distributed without significant overlap on the black-shale bedding planes. Fine laminae, prevailing
174 in the enclosing shales, surround the lenticular form (LF) specimens investigated here with a
175 selection illustrated in Fig. 3 and Fig. S1. This indicates that the structures were in place before burial
176 compaction as illustrated in Fig. 4. Most specimens are filled with fine-grained sediments, yet some
177 are only represented as impressions. Both molds and impressions are commonly preserved in three
178 dimensions.

179

180 **3. Materials and Methods**

181 About 300 LF specimens with exquisitely preserved morphologies were collected from the FB2b
182 subunit at the Moulendé Quarry within a ~5m thick black-shale layer dominated by silts and clays
183 (El Albani et al., 2010; El Albani et al., 2019). They were photographed at the University of Poitiers
184 using a Nikon Europe D610 digital single-lens reflex camera equipped with a Nikon AF-S 24-120 mm
185 f/4G ED VR lens. The textural contrasts between a given LF specimen's filling and its host rock were
186 investigated on polished slab sections with a ZEISS Discovery V8 stereoscope coupled with an Axio
187 Cam ERc 5s microscope camera.

188

189 Described as one of the largest Paleoproterozoic accumulations of organic matter in the world and
190 based on their high total organic carbon (TOC) at current high maturity (Mossman, 2001), the FB
191 black shales are widely regarded as the source rocks of the remarkably large oil field of Franceville.
192 Liquid hydrocarbon, the remnants of which have since solidified, was generated through the "oil
193 window" (<100°C) (Mossman et al., 2005). Such low temperatures make Raman geothermometers
194 unsuitable to assess the intensity of metamorphism. Beyssac et al.'s (2002; 2003) thermometer is
195 best calibrated above 300°C, while the peak-width thermometer of Kouketsu et al. (2014) is
196 unreliable below 150°C and has an uncertainty of ±50°C. In addition, the Raman spectra of organic
197 carbon depends not only on the maximum temperature but also on the nature of organic precursor
198 (Quirico et al., 2009). In particular, Phanerozoic organic material cannot be used as reference for
199 establishing temperatures on early sediments. Raman spectra were therefore not obtained.

200

201 *3.1 Synchrotron radiation induced X-ray fluorescence (SR-XRF) analysis*

202 Polished slab sections of representative samples were chosen for scanning X-ray fluorescence
203 analysis. The SR-XRF measurements were performed on several areas within the studied samples at
204 the Nanoscopium hard X-ray nanoprobe beamline (Somogyi et al., 2015) at Synchrotron Soleil,
205 France. The monochromatic X-ray beam of 18 keV energy was focused on the sample area by a
206 Kirckpatrick-Baez nano-focusing mirror. Micrometer resolution for elemental maps of mm²-sized

207 sample areas was obtained by implementing the fast continuous scanning (FLYSCAN) technique. Full
208 XRF spectra were collected for each pixel of the scans by two Si-drift detectors (VITUS H50, KETEK
209 GmbH) in order to increase the solid angle of detection. The XRF sum-spectra of the measured
210 regions were fitted by the PyMCA software (Solé et al., 2007) to identify the elements detectable in
211 the samples. The spatial distribution of the identified elements, S, K, Ca, Ba, Mn, Fe, Ni, Cu, Zn, Ga,
212 Ge, As, Se, Pb, Sr, and Zr, was reconstructed by a home-made Matlab code, which also corrects for
213 spectral overlapping. Each elemental intensity map was then corrected for the variation of the
214 incoming X-ray intensity and measurement dead-time and was normalized to 10 ms/pixel exposure
215 time. The semi-quantification of the elemental distribution maps was obtained by a home-made
216 Matlab code converting the measured intensity distributions into mass fractions by using calibration
217 factors obtained by measuring a known sample in the same measurement conditions.

218

219 *3.2 X-ray microtomography*

220 Micro-computed tomography (microtomography or micro-CT) analyses were done at the University
221 of Poitiers on an RX-solutions EasyTom XL Duo equipment, which has one micro- and one nanofocus
222 (LaB6 filament) Hamamatsu X-ray source coupled to a Varian PaxScan 2520DX flat panel.
223 Reconstructions were done with the XAct software (RX-solutions) using a classical filtered back
224 projection algorithm and reduction of beam hardening artefact. Virtual sections, 3D rendering, and
225 videos were done with Avizo Fire v.9.2 (FEI).

226

227 *3.3 X-ray diffraction*

228 Approximately the same quantity of whole-rock powder and clay mineral fraction (<2 µm) from 28
229 samples (14 LF fillings and 14 samples of their host rock) were analyzed with a Bruker D8 ADVANCE
230 diffractometer at the University of Poitiers using CuK α radiation operating at 40 kV and 40 mA. The
231 <2 µm clay fraction was separated by dispersion of gently hand-crushed bulk samples in deionized
232 water with an Elma S60 ultrasonic agitation device without any chemical pre-treatment. The
233 dispersed particles were allowed to settle under gravity at a controlled room temperature of 20°C
234 and centrifuged to separate the <2 µm clay fraction. Oriented slides were prepared by drying ~1 mL
235 of suspension on glass slides at room temperature. Analysis of whole-rock powder samples was
236 performed over an angular range of 2-65° 2 θ with a step size of 0.025° 2 θ per 3 s. Oriented slides of
237 the <2 µm clay fraction were analyzed at a step size of 0.02° 2 θ per 3 s counting time and over 2 to
238 30° 2 θ angular range after successive air drying (AD) and ethylene glycol (EG) saturation. Oriented
239 samples were then prepared and analyzed in AD and EG states. Background stripping, indexing of
240 peaks, and mineral identification were done using Bruker Eva software by comparing with
241 International Centre for Diffraction Data (ICDD) files. The results were compared with reference data
242 }. We fitted one experimental sample from each lithology (LF fillings and host rock) in AD and EG
243 states. Instrumental and experimental factors, such as the divergence slit, goniometer radius, soller
244 slits, sample length, and quartz reference intensity, which are specific to the Bruker D8 ADVANCE
245 diffractometer, were introduced. Sigmastar and the mass adsorption coefficient for Cu radiation
246 were set to 13 and 45 cm² g⁻¹, respectively.

247

248 *3.4 Electron microscopy*

249 Samples were carbon coated and imaged with an FEI Quanta 200 scanning electron microscope
250 (SEM) equipped with an energy-dispersive X-ray spectrometer (EDX) at the Universities of Poitiers
251 and Lille. Mineral identification and documentation of textural relationships were acquired in back-
252 scattered electron mode (BSE) operated at an accelerating voltage of 15 kV, 1 nA beam current, and
253 a working distance of 10.5 mm.

254

255 *3.5 Whole-rock chemical analysis*

256 Major, trace, and rare-earth element abundances were determined on 14 LF fillings (specimens) and
257 14 host rock samples (the host sediments) at Service d'Analyse des Roches et Minéraux (SARM) of
258 the Centre de Recherches Pétrographiques et Géochimiques (CRPG), Nancy, France, following the
259 technique described by Carignan et al. (2001).

260

261 *3.6 Carbon abundance and $\delta^{13}\text{C}$ analysis*

262 Fourteen LF fillings and 14 host rock samples were powdered for the measurement of organic
263 matter content. A FlashEA 1112 (ThermoFisher Scientific) CHNS analyser was used for flash dynamic
264 combustion at 970°C under a constant helium flow. The Eager 300 software was used for data
265 acquisition. A calibration curve was performed with aspartic acid and nicotinamide before each
266 analysis. The measured carbon content includes both inorganic and organic carbon, but whole-rock
267 geochemical data show that CaO contents are low. The analytical technique used for $\delta^{13}\text{C}$ analysis
268 was described by Mercuzot et al. (2021).

269

270 *3.7 Zinc and lead isotope analysis*

271 Lead and Zn were separated by anion-exchange column chromatography and their isotopic
272 compositions measured by multiple-collector inductively coupled plasma mass spectrometry (MC-
273 ICP-MS) at the Ecole Normale Supérieure de Lyon (ENS Lyon). Ultrapure water and distilled nitric
274 acid (HNO_3), hydrochloric acid (HCl), and hydrobromic acid (HBr) were used throughout.

275

276 About 100 mg of bulk sample was digested in a Savillex PFA beaker using 3 mL concentrated HCl and
277 0.5 mL concentrated HNO_3 at 100°C for 72 h. After evaporation to dryness, 2 mL concentrated HCl
278 were added for a second round of digestion at 100°C for 24 h. The digested sample was evaporated
279 to dryness and redissolved in 0.2 mL 2M HBr at 100°C for 2 h, evaporated to dryness, and redissolved
280 in 1 mL 2M HBr for chromatographic separation of Pb and Zn on micro-columns filled with 0.5 mL
281 new Biorad AG1-X8 (100-200 mesh). Samples were centrifuged prior to loading the supernatant
282 onto the anion-exchange columns, which had been cleaned with 6M HCl and preconditioned with
283 2M HBr. The sample matrix was discarded with 3 mL 2M HBr, while Pb was eluted with 3 mL 6M HCl
284 and Zn was eluted with 3 mL 0.5M HNO_3 . Zinc was purified a second time following the same elution
285 protocol. The procedural blanks were <300 pg (Pb) and <30 ng (Zn).

286

287 The Pb isotope compositions were analyzed on a Nu Plasma 500 HR MC-ICP-MS at ENS Lyon using a
288 DSN100 desolvation nebulizer system. Samples were dissolved in distilled 0.05M HNO_3 with 5 ppb
289 Tl and concentrations were adjusted to 30 ppb. Instrumental mass bias was corrected using Tl while

290 the accuracy of the measurements was adjusted by sample-standard bracketing relative to NIST
291 SRM 981 (the Pb isotopic Standard Reference Material (SRM) 981 from the National Institute of
292 Standards and Technology (NIST)) (Albarède et al., 2004). NIST 981 was measured systematically
293 every second sample throughout each individual run session allowing for a final normalization to
294 the double-spike values of Eisele et al. (2003). The repeated measurements of NIST SRM 981 yielded
295 an external reproducibility < 100 ppm (0.01%) for ²⁰⁴Pb-normalized ratios and < 50 ppm (0.005%)
296 for ²⁰⁷Pb/²⁰⁶Pb and ²⁰⁸Pb/²⁰⁶Pb. Zinc isotope abundances also were analyzed on the Nu Plasma 500
297 HR MC-ICP-MS at ENS Lyon but without desolvation. Instrumental mass bias was corrected using Cu
298 NIST SRM 976 and sample-standard bracketing (Albarède et al., 2004). Zinc concentrations were
299 adjusted to 200 ppb by dilution with 0.05M HNO₃. The Zn isotopic compositions are reported in
300 parts per 1000 relative to the Lyon JMC in-house standard in delta notation. Typical δ⁶⁶Zn error bars
301 are 0.05‰.

302

303 4. Results

304 4.1 Sample morphology

305 Visual observation (Figs. 3 and 4) and X-ray tomography reveal lenticular to circular shapes with
306 radial symmetry (Fig. S1). Many specimens are rimmed by a mm-wide brim (Fig. 2 and Fig. 3), with
307 a width proportional to the object size. The significance of samples with and without brims is
308 unclear. Some specimens presented in Fig. 3 and Fig. S1 further show a radial pattern. Whether this
309 pattern signals the presence of internal compartments in some individuals or a particular
310 mechanical behavior of the LF will be discussed in a separate paper. Back-scattered electron and
311 microtomography images of cross-sections demonstrate that the LF deflect the underlying
312 sedimentary laminae (Fig. 4). Their diameters vary systematically with stratigraphic height (Fig. 5),
313 ranging from 0.2 to 1 cm at the bottom of the black-shale layer and continue to increase
314 systematically to >3 cm (almost 4 cm) at the top of the succession.

315

316 4.2 Grain size and mineralogy

317 Based on scanning electron microscopy-back-scattered electron imaging (SEM-BSE) coupled to
318 energy-dispersive X-ray spectrometry (EDX), the LF show a stark contrast with its host sediments
319 (Fig. 6). The LF have a fine-grained composition, with a sharp contact with the host sediments. The
320 composition of the LF is typically enriched in clay minerals and organic carbon content. Metal
321 sulfides and carbonate minerals are absent. The clay minerals are parallel to the bedding and aligned
322 along the perimeter of the specimens. This relationship confirms pre-compactional formation of the
323 LF, resulting in local rearrangement of sediment grains during compaction. In this regard,
324 taphonomical preservation occurred during early burial by the decay of organic matter leading to
325 the complexation of organic matter with hydrous fine-sized clay minerals uniformly filling the
326 available space provided by the LF.

327

328 The bulk X-ray mineralogical data on both the fillings and the host black shales show the presence
329 of quartz, micas, illite, chlorite, and other clay minerals (Fig. 6 and Fig. S2). The grain-size of the LF
330 is clearly finer than that of the host rock (Fig. 6). Smectite is particularly abundant within the LF.

331 Very few detrital minerals (e.g., quartz, micas) are scattered within the LF, whereas a matrix of mixed
332 organic material and clays is pervasive to the whole specimen.

333

334 4.3 Geochemistry

335 Figures 7a-d reveal important geochemical features of the LF and their host rock. First, Pb isotope
336 compositions were measured on two different fractions of the 14 samples: (1) a clay fraction largely
337 composed of the LF fillings, and (2) a fraction of the host sediment (Table S1). In $^{207}\text{Pb}/^{206}\text{Pb}$ -
338 $^{204}\text{Pb}/^{206}\text{Pb}$ space, all the data points define a linear array with a robust age of 1890 ± 100 Ma (2-
339 sigma error) (Fig. 7a) consistent with literature data (Bonhomme et al., 1982; Bros et al., 1992;
340 Gauthier-Lafaye et al., 1996). The absolute age is key to assessing whether the Pb-Pb age refers to
341 a diachronous Lomagundi or a post-Lomagundi event (see Supplementary Information for details).
342 Both the alignment itself and the age of the alignment confirm that if diagenesis had affected these
343 samples, it could only have been *shortly after* sediment deposition of the Francevillian series.

344

345 Second, as summarized in Table 1 from the complete data set listed in Supplementary Tables- S1-S3
346 and shown in Figs. 7a-d, the marked geochemical and isotopic contrasts between the LF and their
347 host rock are statistically robust and significant. The LF are characterized by higher Lu/Hf ratios and
348 have higher concentrations of organic C and Zn, but contain less Si, K, Zr, and Hf than their host rock.
349 The Zn contents of the host rock are consistent with the range observed for other black shales
350 worldwide over the last 2.7 Ga (Scott et al., 2013) with the consistency being linked to organic
351 complexes playing an important role in controlling Zn solubility through time (Robbins et al., 2013).
352 The Zn excess (x_s) in the fillings (fil) can be calculated by subtracting a Zn component chemically
353 similar to the host rock (hr) from the total concentration. With elemental Fe in organic material
354 being negligible, this gives the simple relationship $[\text{Zn}]_{x_s} = [\text{Zn}]_{fil} - (\text{Zn}/\text{Fe})_{hr} \times [\text{Fe}]_{fil}$, where brackets refer
355 to concentrations. The average Zn_{x_s} values in nine specimens is 111 ± 44 ppm. Consistent Zn excess
356 values are obtained by replacing Fe with other lithogenic elements, such as Y, Zr, Al, or Ti (97-
357 140 ppm).

358

359 Zinc is isotopically lighter and Pb more radiogenic in the LF with respect to their host rock. The $\delta^{66}\text{Zn}$
360 values of the LF host rock average $0.36\pm 0.10\text{‰}$ (1 sigma) (Table S1), which is well within the
361 lithogenic range (Moynier et al., 2017) but in stark contrast to the average $\delta^{66}\text{Zn}$ of the LF fillings of
362 $0.10\pm 0.10\text{‰}$, which a t -test shows to be highly statistically significant ($p=7\times 10^{-7}$) (Figs. 7b and d,
363 Table S1).

364

365 The $\delta^{13}\text{C}$ of a selection of carbon fractions (Table S4) shows no significant difference between the
366 fillings and the host sediments. The average $\delta^{13}\text{C}$ value ($-34.5\pm 0.5\text{‰}$) is consistent with Canfield et
367 al.'s (2013) data and falls well within the range of Proterozoic kerogen samples (Des Marais, 1997).

368

369 5. Discussion

370 5.1 Diagenesis

371 A preliminary issue about the present data set is whether the original geochemistry of the LF and
372 their host rock material has been reset by metamorphism or diagenesis. Iconic Cambrian

373 Lagerstätten, such as the Burgess Shale and Siriuspasset fossil assemblages, were buried to
374 temperatures of ~300°C, typical of greenschist facies (Butterfield et al., 2007; Gaines et al., 2019;
375 Powell, 2003), which would have been detrimental to the preservation of a primary geochemical
376 signal. By contrast, the Francevillian black shales still contain smectite-rich clays with randomly
377 mixed layers, which attest to a very low diagenetic grade. Persisting smectite relicts within illite at
378 the burial stage limit the temperature of diagenesis to <80°C (Velde and Vasseur, 1992). This
379 observation is consistent with the maturation of the abundant organic material present in the FB
380 within the oil formation window (<100°C).

381

382 The preservation of an isochronous relationship with the correct geological age indicates that the
383 U-Th-Pb system was not reset by any event potentially taking place after early diagenesis. By
384 extension it can therefore confidently be assumed that neither were Zn isotopes. Over nearly five
385 decades, several authors have pointed out that Co fluxes to oceanic sediments have remained
386 constant over the last 200 Ma (Dunlea et al., 2015; Krishnaswami, 1976; Zhou and Kyte, 1992).
387 Thibon et al. (2019) demonstrated on cores from the pre-GOE Transvaal Supergroup, South Africa,
388 that Co relative chronometry can be used to estimate sedimentation rates that are within 50% of
389 the rates provided by zircon U-Pb chronology. In order to calculate the time interval Δt during which
390 a series of sediments with thickness Δd (in meters), dry bulk density ρ_{sed} (in g cm^{-3}), and Co
391 concentration [Co] (in ppm) is deposited, they used the mass-conservation relationship:

392

$$\Delta t = \rho_{\text{sed}} [\text{Co}] \Delta d / Q_{\text{Co}}$$

393

394 where Q_{Co} is the modern cobalt deposition rate of $3600 \mu\text{g cm}^{-2} \text{Ma}^{-1}$ (Thibon et al., 2019). With all
395 due caution taken with respect to the uncertainties associated with this technique, this expression
396 suggests that the ~5 m-thick layer of black shales hosting the LF specimens was deposited in about
397 20,000 years (25 cm ka^{-1}). In the modern ocean, such rapid sedimentation rates are observed along
398 passive margins and in the distal parts of the Bengal and Indus fans (Dutkiewicz et al., 2016)

399

400 5.2 *The lenticular forms are neither secondary features nor concretions*

401 The LF are not syn-depositional or secondary features formed during burial. Morphology shows that
402 the LF are pre-compaction features that cannot be confused with concretions for two reasons: (1)
403 the brim width is proportional to the size of the specimen, which argues against control by diffusion;
404 and (2) Fig. 4 shows that the silt laminae below the specimen are visibly deflected. The geochemical
405 contrast between the LF and their host rock therefore predates compaction. The persistence of this
406 contrast through diagenesis indicates that only the finest clay material could infiltrate what must
407 have been the LF cavity.

408

409 Microtomography shows that the minerals of the brims are the same as those present in the host
410 rock and the interior of the LF (Fig. 4b). The remarkably constant ratio of brim to external diameter
411 of 0.15 ± 0.04 (Fig. 5 inset) over a range of external diameters of 0.2 to 4 cm is consistent with a
412 simple principle of comparative anatomy: for a given species and regardless of the size of
413 individuals, the relative proportions between anatomic units tend to remain similar. If the brims
414

415 represented diffusion boundary layers, they would be scaled by external physical and chemical
416 parameters, typically in the form of $(Dt)^{1/2}$, with t being the duration of the exchange and
417 temperature-dependent D the diffusion coefficient of the elements moving in and out of the form.
418 The brims would in this case be expected to have the same width in any given layer which is not
419 what is observed.

420

421 The distinctly lenticular shape of these objects and the regular progression of their size over time
422 are therefore better reconciled with a biological origin than a sedimentary phenomenon such as
423 minute mud volcanoes or sedimentary nodules.

424

425 Finally, should diagenesis from fluid circulation have affected the geochemistry in general, and the
426 Zn isotopes in particular, both the host rock and the LF would have been affected. Post-mortem
427 infiltration of fine-grained sediment into the LF inner cavity should not be mistaken for diagenetic
428 modification. Even in hand specimens, the LF appear as distinct bodies with sharp convex outlines
429 in every dimension, so much so that individual LF are easily freed from their host rock (Fig. 3, Fig. 2
430 and Fig. S1). As for most bona fide macroscopic fossils, such an effortless release of the LF indicates
431 a strong rheological discontinuity and the lack of a diffusion rim. The fact that Zn and C
432 concentrations and Zn isotopes in the interior of the forms are anomalous with respect to the host
433 rock is evidence that the LF were buried with their geochemical anomaly already in place.

434

435 *5.3 Pyritization of the circular forms is an uncommon local feature associated with fractures*

436 Sedimentary pyrite is formed by either syngenetic precipitation of minute crystals when at least
437 some layers of the water column are euxinic or during diagenetic sulfate reduction (Canfield et al.,
438 1996; Shen et al., 2002).-The scatter of micron-sized pyrite crystals (illustrated by, for example, the
439 Fe and S distribution in Fig. S3 does not support sulfate reduction except along some rare
440 stratigraphic diastems which favor water flow. The bimodal grain size of pyrite crystals strongly
441 argues against pyrite dissolution during diagenetic evolution. Disseminated tiny pyrite crystals (1-3
442 μm) persist in the matrix next to larger crystals ($>30 \mu\text{m}$). Because of their high surface energy, small
443 crystals are much more soluble than large crystals. When diagenetic fluids percolate, small crystals
444 dissolve and redeposit onto larger crystals, a mechanism known as Ostwald ripening. Most $\delta^{34}\text{S}$
445 values in both disseminated pyrite (about $-25 \pm 5 \text{‰}$ (El Albani et al., 2014)) and large crystals (>30
446 μm) are consistent with the net burial of organic material (Planavsky et al., 2012). Much less
447 frequent $\delta^{34}\text{S}$ values $> -20 \text{‰}$ may occur at the periphery of large pyrite crystals growing along
448 fractures.

449

450 Mass balance also requires that the modal proportion of pyrite in the samples is very small: making
451 the extreme assumption that all S in the sample is in the form of pyrite (i.e., no S in the matrix) and
452 dividing the maximum S concentration in the sample (3000 ppm, Table S3) by the S concentration
453 in pyrite ($\sim 36 \text{ wt.}\%$), the maximum weight proportion of pyrite is 0.8%. This is in excellent agreement
454 with the $\sim 1\%$ pyrite micro-crystals detected by synchrotron-based scanning X-ray fluorescence
455 microscopy (SR-XRF) imaging (Fig. S3 and Fig. S4). SR-XRF data indicate that the actual Zn
456 concentration in pyrite is in the range of $< 100 \text{ ppm}$. Scarcity of pyrite has also been pointed out in

457 the Burgess Shale by Anderson et al. (2021). Even if an extreme value of 2000 ppm Zn in sedimentary
458 pyrite (Large et al., 2014) is adopted, the calculated pyrite abundance would only account for 15
459 ppm of the rock's Zn inventory, which is insufficient to explain the anomalously light $\delta^{66}\text{Zn}$ values of
460 the LF fillings (see below). The suggestion (Conway and John, 2014; Little et al., 2016) that diagenetic
461 fluids cause loss of isotopically heavy Zn associated with the formation of modern sedimentary
462 sulfides therefore is not applicable to the Francevillian black shales. Sulfate reduction to pyrite is
463 *not* the process controlling the Zn budget or the Zn isotopic compositions of these samples.

464

465 The distinctive Zn anomalies cannot be explained by pyritization either. The large Zn excesses (~ 100
466 ppm) observed in the fillings of the LF are not supported by the rare minute crystals of pyrite
467 observed by SR-XRF (Fig. S3). The distribution maps of S, K, Ca, and Mn do not show any significant
468 co-localization with Zn (see Fig. S5). It can therefore be concluded that Zn is not linked to S, K, Ca,
469 or Mn-containing mineral phases whether in the LF or the host rocks. High-resolution Zn, Fe, and S
470 concentration maps at a micron-scale resolution and ppm-range sensitivity across the specimens
471 distinctly show that the Zn/Fe ratios in pyrite are about two orders of magnitude smaller than the
472 ratios in the matrix. Pyrite crystals are definitely not Zn hot-spots. In addition, the spatial dispersion
473 of Zn throughout the black shales shows that Zn excesses within the LF fillings are randomly
474 distributed across the sample. They follow a Poisson distribution (Fig. 8), and, with rare exceptions,
475 do not follow stratification or fractures.

476

477 *5.4 The biological nature of the lenticular forms*

478 The singular behavior of Zn, an element particularly abundant in cellular interiors, is correlated with
479 LF organic carbon. Figure 6c shows how C contents correlate with Zn contents after normalization
480 to Al to account for variable clay abundances. The atomic C/P ratio in the interior of the LF objects
481 is in general high, up to about 140 (average $\sim 95 \pm 27$, 1 sigma) and is consistent with the Redfield
482 ratio of modern eukaryotes (Körtzinger et al., 2001). The average $\delta^{13}\text{C}$ value of $-34.5 \pm 0.5\%$ confirms
483 the lack of major organic carbon oxidation.

484

485 With sulfate reduction being dismissed, the most parsimonious explanation for the Zn excesses
486 observed in the fillings of the LF specimens is via an organic carrier. The Zn/Al ratio is up to a factor
487 of 4.3 higher (2.3 on average) in the fillings relative to their host rock and correlates with C content
488 (Fig. 7c). The proportion f_{xs} of organic-bound Zn in the fillings is also remarkably constant at 61 ± 8
489 wt.%. Such Zn excess values are well within the range of Zn concentrations measured in modern
490 dry phytoplankton (Collier and Edmond, 1984).

491

492 $\delta^{66}\text{Zn}$ values of Archean and Proterozoic pyrite have been shown to be indistinguishable from the
493 lithogenic range (Isson and Planavsky, 2018), which reflects that sulfide minerals do not
494 fractionate Zn isotopes with respect to seawater (Fujii et al., 2014). By contrast, isotopically light
495 Zn isotopes preferentially bind to sulfur-rich amino acid (notably cysteine) (Fujii et al., 2014;
496 Moynier et al., 2017). By subtracting, as above, the host-rock component and taking the mass-
497 balance condition $\delta^{66}\text{Zn}_{xs} = [\delta^{66}\text{Zn}_{fil} - (1 - f_{xs}) \delta^{66}\text{Zn}_{hr}] / f_{xs}$ into account, the mean $\delta^{66}\text{Zn}$ of the organic
498 component of the LF fillings is estimated to be $-0.08 \pm 0.20\%$, a value about 0.4% lighter than the

499 value of lithogenic Zn, which for an element as relatively heavy as Zn is a substantial shift. Such a
500 low value is consistent with the range of $\delta^{66}\text{Zn}$ obtained from phytoplankton cultured in seawater
501 (Köbberich and Vance, 2019; Samanta et al., 2018), and with Archean and Proterozoic kerogen
502 (Isson et al., 2018). The systematically lighter $\delta^{66}\text{Zn}$ values of the LF fillings with respect to their
503 host rock therefore indicate that organic material in the LF fillings is not due to infiltration of liquid
504 hydrocarbons but represent primary organic material.

505

506 A back-of-the-envelope calculation rooted in the concept of ‘minimum Zn quota’, which is the
507 lowest amount of zinc per cell that allows for optimal growth (Outten and O’Halloran, 2001), drives
508 home the point that significant phytoplankton biomass was incorporated into the LF. For example,
509 assuming 100 ppm Zn excess in the LF (Table 1), which can be conservatively represented by a 0.1 x
510 1.0 cm cylinder with a density of 2.5 g cm^{-3} , leads to $3.33 \text{ }\mu\text{M Zn}$. Based on the Zn content of a
511 modern anoxygenic photoautotroph (Konhauser et al., 2018), where one cell has $8.08 \times 10^{-18} \text{ mol}$
512 Zn, then $3.33 \text{ }\mu\text{M Zn}$ require 4.1×10^{11} cells. If the mass of the LF was 77.5 mg ($0.031 \text{ cm}^3 \times 2.5 \text{ g cm}^{-3}$),
513 then 5.3×10^9 cells were required for each mg of LF. To put this number into context, humans
514 have an estimated 37 trillion cells (Bianconi et al., 2013), which, based on a 70 kg person, is
515 equivalent to $5.3 \times 10^8 \text{ cells mg}^{-1}$.

516

517 Zinc excesses, high C/P ratios, and low $\delta^{66}\text{Zn}$ in the LF fillings therefore concur to show that the LF
518 inherited abundant material of organic origin. Infiltration of fine clay mineral into the cavity was
519 probably facilitated by post-mortem bloating of the LF. Zinc is a particularly widespread co-factor of
520 a large number of proteins and a micronutrient of phytoplankton (Moore et al., 2013). Irrespective
521 of whether the LF were prokaryotic or eukaryotic, the present observations validate Zn excesses and
522 Zn isotopes as robust biosignatures consistent with morphological criteria.

523

524 The exact kind of life form that the LF represent will be addressed in detail in a separate manuscript,
525 but we will allow ourselves some preliminary speculation here. The internal organic material may
526 consist of cyanobacteria carrion harvested in the nepheloid layer. The presence of a brim therefore
527 suggests that the LF were floating in the water column. This way of living is supported by their
528 settling on different type of substrata. The LF could represent the remnants of prokaryote gigantism,
529 in which case they would be the largest bacteria on record, more than an order of magnitude than
530 the biggest extant species (e.g., up to $750 \text{ }\mu\text{m}$ for *Thiomargarita namibiensis* (Schulz and Jørgensen,
531 2001)). It is conceivable that the early appearance gigantism of the LF is in some way related to the
532 underlying Oklo natural nuclear reactors that would have heated the deep interstitial waters and
533 thereby triggered the convection of diagenetic fluids and favored extraction (leaching) of nutrients
534 by interaction of seawater with the host rock.

535

536 More fittingly though, the LF could be eukaryotes, which are often suggested to have appeared 300
537 My later in the early Mesoproterozoic (Knoll et al., 2006). A caveat is that the date of eukaryote
538 emergence is contingent on the reliability of molecular clocks (Butterfield, 2015) and scant field
539 observations. The LF could represent one of the earliest organisms hypothesized by some authors
540 (Javaux and Lepot, 2018; Knoll, 2014), in this case a soft epibenthic eukaryote. A large variety of cm-

541 sized single-cell organisms using sediment grains to build a delicate agglutinated shell exist in the
542 modern abyssal ocean (Gooday et al., 2017). Agglutination of silt material, which appeared multiple
543 times in the evolutionary history of protists (Bowser et al., 2006), would explain the preservation of
544 LF morphological details through fossilization. Given the multiple biological requirements for Zn, its
545 concomitant increase in concentration and LF size up strata may simply reflect the greater Zn
546 demand with increasing cell volume.

547 **6. Conclusions**

548 The geochemical features of ~2 Ga old objects in Francevillian sediments demonstrate their
549 biogenicity under conditions that may be more typical of deep time on Earth and other planets than
550 the extremely differentiated faunas from the Late Proterozoic and the Early Cambrian. We have
551 reached the following conclusions:

- 552 a. Diagenetic changes were limited and largely without effect on the mineralogy of the
553 Francevillian LF. Most non-volatile elements, including Pb and Zn and their isotope
554 systematics, were left unchanged.
- 555 b. The LF are clearly not concretions or secondary features. The stark geochemical contrasts
556 between the host rock and the LF fillings, notably those associated with Zn, were buried with
557 the LF.
- 558 c. Pyritization, when present, is limited to rare fractures and does not affect the bulk of sulfur
559 concentrated in the organic material and leaves the Zn budget largely unaffected.
- 560 d. The criteria used in this work are heavily biased towards geochemical observations and
561 demonstrate the biogenic nature of the lenticular forms. These organisms probably
562 represent clay-clad protists of exceptionally large size.

563e. The decision tree leading to infer the biogenicity of the Francevillian LF may be extended in deep
564 time to other sedimentary features, while the approach itself of investigating biogenicity of
565 fossilized remnants using Zn isotopes together with other isotopes (e.g., S and C) and organic
566 tracers, may be extended to extraterrestrial samples.

567

568

569 **Author Contributions:** A.E.A. designed the research. A.E.A., F.A., J.B.T., A.S., E.C.F. and K.O.K. wrote
570 the manuscript. A.E.A, E.C.F, and J.N.G did the field work. J.N.G., C.F., J.N.G., and A.E.A. prepared
571 the samples and performed XRD analyses and models. A.M. performed X-Ray microtomography.
572 A.E.A. analyzed morphology, A.R. analyzed carbon and sulfur concentrations. A.C.P.W. analyzed
573 carbon isotopes. A.L. analyzed Zn and Pb isotope compositions with assistance from J.B.T. A.S
574 carried out the synchrotron experiments and processed the data.

575 **Acknowledgments**

576 We thank the Gabonese government, the Region Nouvelle Aquitaine, the Centre National pour la
577 Recherche Scientifique and Technique du Gabon (CENAREST), the General Direction of Mines and
578 Geology of Gabon, the Sylvia Bongo Ondimba Foundation, the Agence Nationale des Parcs
579 Nationaux du Gabon, the University of Masuku, the COMILOG and SOCOBA Companies, the French
580 Embassy at Libreville, the Institut Français du Gabon, and the Centre National de la Recherche
581 Scientifique (CNRS) for their support, and ENS Lyon for providing access to laboratories and

582 equipment for chemical and isotopic analysis. Discussions with Bruno Reynard were very helpful to
583 assess the relevance of Raman spectroscopy in evaluating metamorphic temperatures in ancient
584 sediments. We thank the CT μ platform (University Lyon 1) for access to SEM. We thank K. Medjoubi
585 for his contribution to the SR-XRF measurements, for developing Matlab codes for data treatment,
586 and for scientific discussions. We thank S. Bengtson, L. White, P.-D. Mougouama, R. Oslisly, A.
587 Meunier, A. Trentesaux, O. Bankole, J. Aubineau, B. Becker, J. Vannier, J.C. Baloche, F. Weber, F.
588 Gauthier-Lafaye, F. Pambo, J.L. Albert, and Andy Knoll for geological information and scientific
589 discussion, and C. Lebailly, L. Tromas, P. Télouk, C. Laforest, C. Boissard, Ph. Recourt, and S. Ventalon
590 for technical assistance. We thank two reviewers for useful suggestions that allowed us to clarify
591 some points of the manuscript.

592

593

594

595

596 **References**

- 597 Albarède, F., Telouk, P., Blichert-Toft, J., Boyet, M., Agranier, A., Nelson, B., 2004. Precise and accurate
598 isotopic measurements using multiple-collector ICPMS. *Geochim. Cosmochim. Acta* 68, 2725-2744.
- 599 Allwood, A.C., Rosing, M.T., Flannery, D.T., Hurowitz, J.A., Heirwegh, C.M., 2018. Reassessing evidence of life
600 in 3,700-million-year-old rocks of Greenland. *Nature* 563, 241-244.
- 601 Anderson, R.P., Tosca, N.J., Saupe, E.E., Wade, J., Briggs, D.E., 2021. Early formation and taphonomic
602 significance of kaolinite associated with Burgess Shale fossils. *Geology* 49, 355-359.
- 603 Beyssac, O., Brunet, F., Petitet, J.-P., Goffé, B., Rouzaud, J.-N., 2003. Experimental study of the microtextural
604 and structural transformations of carbonaceous materials under pressure and temperature. *European*
605 *Journal of Mineralogy* 15, 937-951.
- 606 Beyssac, O., Goffé, B., Chopin, C., Rouzaud, J., 2002. Raman spectra of carbonaceous material in
607 metasediments: a new geothermometer. *Journal of metamorphic Geology* 20, 859-871.
- 608 Bianconi, E., Piovesan, A., Facchin, F., Beraudi, A., Casadei, R., Frabetti, F., Vitale, L., Pelleri, M.C., Tassani, S.,
609 Piva, F., 2013. An estimation of the number of cells in the human body. *Annals of human biology* 40, 463-
610 471.
- 611 Bonhomme, M., Gauthier-Lafaye, F., Weber, F., 1982. An example of Lower Proterozoic sediments: the
612 Francevillian in Gabon. *Precambrian Research* 18, 87-102.
- 613 Bowser, S.S., Habura, A., Pawlowski, J., Katz, L., Bhattacharya, D., 2006. Molecular evolution of Foraminifera.
614 *Genomics and evolution of microbial eukaryotes*, 78-93.
- 615 Bros, R., Stille, P., Gauthier-Lafaye, F., Weber, F., Clauer, N., 1992. Sm-Nd isotopic dating of Proterozoic clay
616 material: An example from the Francevillian sedimentary series, Gabon. *Earth and Planetary Science Letters*
617 113, 207-218.
- 618 Butterfield, N.J., 2007. Macroevolution and macroecology through deep time. *Palaeontology* 50, 41-55.
- 619 Butterfield, N.J., 2015. Early evolution of the Eukaryota. *Palaeontology* 58, 5-17.
- 620 Butterfield, N.J., Balthasar, U., Wilson, L.A., 2007. Fossil diagenesis in the Burgess Shale. *Palaeontology* 50,
621 537-543.
- 622 Canfield, D.E., Lyons, T.W., Raiswell, R., 1996. A model for iron deposition to euxinic Black Sea sediments.
623 *American Journal of Science* 296, 818-834.
- 624 Canfield, D.E., Ngombi-Pemba, L., Hammarlund, E.U., Bengtson, S., Chaussidon, M., Gauthier-Lafaye, F.,
625 Meunier, A., Riboulleau, A., Rollion-Bard, C., Rouxel, O., 2013. Oxygen dynamics in the aftermath of the Great
626 Oxidation of Earth's atmosphere. *Proceedings of the National Academy of Sciences* 110, 16736-16741.
- 627 Carignan, J., Hild, P., Mevelle, G., Morel, J., Yeghicheyan, D., 2001. Routine analyses of trace elements in
628 geological samples using flow injection and low pressure on-line liquid chromatography coupled to ICP-MS:
629 A study of geochemical reference materials BR, DR-N, UB-N, AN-G and GH. *Geostandards Newsletter* 25, 187-
630 198.
- 631 Collier, R.W., Edmond, J.M., 1984. The trace element geochemistry of marine biogenic particulate matter.
632 *Prog. Oceanogr.* 13, 113-199.
- 633 Conway, T.M., John, S.G., 2014. The biogeochemical cycling of zinc and zinc isotopes in the North Atlantic
634 Ocean. *Global Biogeochemical Cycles* 28, 1111-1128.
- 635 Des Marais, D.J., 1997. Isotopic evolution of the biogeochemical carbon cycle during the Proterozoic Eon.
636 *Organic Geochemistry* 27, 185-193.
- 637 Dunlea, A.G., Murray, R.W., Sauvage, J., Pockalny, R.A., Spivack, A.J., Harris, R.N., D'Hondt, S., 2015. Cobalt-
638 based age models of pelagic clay in the South Pacific Gyre. *Geochemistry, Geophysics, Geosystems* 16, 2694-
639 2710.

640 Dutkiewicz, A., Müller, R.D., Hogg, A.M., Spence, P., 2016. Vigorous deep-sea currents cause global anomaly
641 in sediment accumulation in the Southern Ocean. *Geology* 44, 663-666.

642 Eisele, J., Abouchami, W., Galer, S.J.G., Hofmann, A.W., 2003. The 320 kyr Pb isotope evolution of Mauna Kea
643 lavas recorded in the HSDP-2 drill core. *Geochem. Geophys. Geosyst.* 4, doi: 10.1029/2002GC000339.

644 El Albani, A., Bengtson, S., Canfield, D.E., Bekker, A., Macchiarelli, R., Mazurier, A., Hammarlund, E.U.,
645 Boulvais, P., Dupuy, J.-J., Fontaine, C., 2010. Large colonial organisms with coordinated growth in oxygenated
646 environments 2.1 Gyr ago. *Nature* 466, 100-104.

647 El Albani, A., Bengtson, S., Canfield, D.E., Riboulleau, A., Rollion Bard, C., Macchiarelli, R., Ngombi Pemba, L.,
648 Hammarlund, E., Meunier, A., Moubiya Mouele, I., 2014. The 2.1 Ga old Francevillian biota: biogenicity,
649 taphonomy and biodiversity. *PLoS One* 9, e99438.

650 El Albani, A., Mangano, M.G., Buatois, L.A., Bengtson, S., Riboulleau, A., Bekker, A., Konhauser, K., Lyons, T.,
651 Rollion-Bard, C., Bankole, O., 2019. Organism motility in an oxygenated shallow-marine environment 2.1
652 billion years ago. *Proceedings of the National Academy of Sciences* 116, 3431-3436.

653 Fujii, T., Moynier, F., Blichert-Toft, J., Albarede, A.F., 2014. Density functional theory estimation of isotope
654 fractionation of Fe, Ni, Cu, and Zn among species relevant to geochemical and biological environments.
655 *Geochimica and Cosmochimica Acta* 140, 553-576.

656 Gaines, R.R., Lombardo, A.J., Holzer, I.O., Caron, J.-B., 2019. The limits of burgess shale-type preservation:
657 assessing the evidence for preservation of the blood protein hemocyanin in the burgess shale. *Palaios* 34,
658 291-299.

659 Gangidine, A., Walter, M.R., Havig, J.R., Jones, C., Sturmer, D.M., Czaja, A.D., 2021. Trace Element
660 Concentrations Associated with Mid-Paleozoic Microfossils as Biosignatures to Aid in the Search for Life. *Life*
661 11, 142.

662 Gauthier-Lafaye, F., Bros, R., Stille, P., 1996. Pb isotope pe systematics on diagenetic clays: an example from
663 proterozoic black shales of the Franceville basin (Gabon). *Chemical geology* 133, 243-250.

664 Gauthier-Lafaye, F., Weber, F., Ohmoto, H., 1989. Natural fission reactors of Oklo. *Economic Geology* 84,
665 2286-2295.

666 Gooday, A.J., Holzmann, M., Caille, C., Goineau, A., Kamenskaya, O., Weber, A.A.-T., Pawlowski, J., 2017.
667 Giant protists (xenophyophores, Foraminifera) are exceptionally diverse in parts of the abyssal eastern Pacific
668 licensed for polymetallic nodule exploration. *Biological conservation* 207, 106-116.

669 Hickman-Lewis, K., Cavalazzi, B., Sorieul, S., Gautret, P., Foucher, F., Whitehouse, M.J., Jeon, H., Georgelin,
670 T., Cockell, C.S., Westall, F., 2020. Metallomics in deep time and the influence of ocean chemistry on the
671 metabolic landscapes of Earth's earliest ecosystems. *Scientific Reports* 10, 1-16.

672 Hickman-Lewis, K., Garwood, R.J., Brasier, M.D., Goral, T., Jiang, H., McLoughlin, N., Wacey, D., 2016.
673 Carbonaceous microstructures from sedimentary laminated chert within the 3.46 Ga Apex Basalt, Chinaman
674 Creek locality, Pilbara, Western Australia. *Precambrian Research* 278, 161-178.

675 Isson, T.T., Love, G.D., Dupont, C.L., Reinhard, C.T., Zumberge, A.J., Asael, D., Gueguen, B., McCrow, J., Gill,
676 B.C., Owens, J., 2018. Tracking the rise of eukaryotes to ecological dominance with zinc isotopes. *Geobiology*
677 16, 341-352.

678 Isson, T.T., Planavsky, N.J., 2018. Reverse weathering as a long-term stabilizer of marine pH and planetary
679 climate. *Nature* 560, 471-475.

680 Javaux, E.J., Lepot, K., 2018. The Paleoproterozoic fossil record: implications for the evolution of the
681 biosphere during Earth's middle-age. *Earth-Science Reviews* 176, 68-86.

682 Knoll, A.H., 2014. Paleobiological perspectives on early eukaryotic evolution. *Cold Spring Harbor Perspectives*
683 *in Biology* 6, a016121.

684 Knoll, A.H., Javaux, E.J., Hewitt, D., Cohen, P., 2006. Eukaryotic organisms in Proterozoic oceans. *Philosophical*
685 *Transactions of the Royal Society B: Biological Sciences* 361, 1023-1038.

686 Köbberich, M., Vance, D., 2019. Zn isotope fractionation during uptake into marine phytoplankton:
687 implications for oceanic zinc isotopes. *Chemical Geology* 523, 154-161.

688 Konhauser, K.O., Robbins, L.J., Alessi, D.S., Flynn, S.L., Gingras, M.K., Martinez, R.E., Kappler, A., Swanner,
689 E.D., Li, Y.-L., Crowe, S.A., 2018. Phytoplankton contributions to the trace-element composition of
690 Precambrian banded iron formations. *Bulletin* 130, 941-951.

691 Körtzinger, A., Hedges, J.I., Quay, P.D., 2001. Redfield ratios revisited: Removing the biasing effect of
692 anthropogenic CO₂. *Limnology and Oceanography* 46, 964-970.

693 Kouketsu, Y., Mizukami, T., Mori, H., Endo, S., Aoya, M., Hara, H., Nakamura, D., Wallis, S., 2014. A new
694 approach to develop the Raman carbonaceous material geothermometer for low-grade metamorphism
695 using peak width. *Island Arc* 23, 33-50.

696 Krishnaswami, S., 1976. Authigenic transition elements in Pacific pelagic clays. *Geochimica et Cosmochimica*
697 *Acta* 40, 425-434.

698 Large, R.R., Halpin, J.A., Danyushevsky, L.V., Maslennikov, V.V., Bull, S.W., Long, J.A., Gregory, D.D.,
699 Lounejeva, E., Lyons, T.W., Sack, P.J., 2014. Trace element content of sedimentary pyrite as a new proxy for
700 deep-time ocean-atmosphere evolution. *Earth and Planetary Science Letters* 389, 209-220.

701 Little, S.H., Vance, D., McManus, J., Severmann, S., 2016. Key role of continental margin sediments in the
702 oceanic mass balance of Zn and Zn isotopes. *Geology* 44, 207-210.

703 Mänd, K., Lalonde, S.V., Robbins, L.J., Thoby, M., Paiste, K., Kreitsmann, T., Paiste, P., Reinhard, C.T.,
704 Romashkin, A.E., Planavsky, N.J., Kirsimäe, K., Lepland, A., and Konhauser, K.O., 2020. Palaeoproterozoic
705 oxygenated oceans following the Lomagundi-Jatuli Event. *Nature Geoscience* 13, 302-306.

706 Marshall, C.P., Javaux, E.J., Knoll, A.H., Walter, M.R., 2005. Combined micro-Fourier transform infrared (FTIR)
707 spectroscopy and micro-Raman spectroscopy of Proterozoic acritarchs: a new approach to palaeobiology.
708 *Precambrian Research* 138, 208-224.

709 Martin, A.P., Condon, D., Prave, A.R., Melezhik, V.A., Lepland, A., Fallick, A.E., 2013. Dating the termination
710 of the Palaeoproterozoic Lomagundi-Jatuli carbon isotopic event in the North Transfennoscandian
711 Greenstone Belt. *Precambrian Research* 224, 160-168.

712 Martin, A.P., Prave, A., Condon, D., Lepland, A., Fallick, A.E., Romashkin, A., Medvedev, P., Rychanchik, D.,
713 2015. Multiple Palaeoproterozoic carbon burial episodes and excursions. *Earth and Planetary Science Letters*
714 424, 226-236.

715 Melezhik, V.A., Fallick, A.E., Martin, A.P., Condon, D.J., Kump, L.R., Brasier, A.T., 2013., 2013. The greatest
716 perturbation of the global carbon cycle: the Lomagundi-Jatuli isotopic event, in: Melezhik, V., Prave, A.R.,
717 Hanski, E.J., Fallick, A.E., Lepland, A., Kump, L.R., Strauss, H. (Eds.), *Reading the Archive of Earth's*
718 *Oxygenation*. *Frontiers in Earth Sciences*. Springer, Heidelberg, pp. 1111-1150.

719 Mercuzot, M., Thomazo, C., Schnyder, J., Pellenard, P., Baudin, F., Pierson-Wickmann, A.-C., Sans-Jofre, P.,
720 Bourquin, S., Beccaletto, L., Santoni, A.-L., 2021. Carbon and Nitrogen Cycle Dynamic in Continental Late-
721 Carboniferous to Early Permian Basins of Eastern Pangea (Northeastern Massif Central, France). *Frontiers in*
722 *Earth Science*, 615.

723 Moore, C., Mills, M., Arrigo, K., Berman-Frank, I., Bopp, L., Boyd, P., Galbraith, E., Geider, R., Guieu, C., Jaccard,
724 S., 2013. Processes and patterns of oceanic nutrient limitation. *Nature geoscience* 6, 701-710.

725 Mossman, D.J., 2001. Hydrocarbon habitat of the paleoproterozoic Franceville series, republic of Gabon.
726 *Energy sources* 23, 45-53.

727 Mossman, D.J., Gauthier-Lafaye, F., Jackson, S.E., 2005. Black shales, organic matter, ore genesis and
728 hydrocarbon generation in the Paleoproterozoic Franceville Series, Gabon. *Precambrian Research* 137, 253-
729 272.

730 Moynier, F., Vance, D., Fujii, T., Savage, P., 2017. The isotope geochemistry of zinc and copper. *Reviews in*
731 *Mineralogy and Geochemistry* 82, 543-600.

732 Nesbitt, H.W., Young, G.M., 1982. Early Proterozoic climates and plate motions inferred from major element
733 chemistry of lutites. *Nature* 299, 715-717.

734 Neveu, M., Hays, L.E., Voytek, M.A., New, M.H., Schulte, M.D., 2018. The ladder of life detection. *Astrobiology*
735 18, 1375-1402.

736 Olcott Marshall, A., Marshall, C.P., 2015. Vibrational spectroscopy of fossils. *Palaeontology* 58, 201-211.

737 Outten, C.E., O'Halloran, T.V., 2001. Femtomolar sensitivity of metalloregulatory proteins controlling zinc
738 homeostasis. *Science* 292, 2488-2492.

739 Pichat, S., Douchet, C., Albarède, F., 2003. Zinc isotope variations in deep-sea carbonates from the eastern
740 equatorial Pacific over the last 175 ka. *Earth Planet. Sci. Letters* 210, 167-178.

741 Planavsky, N.J., Bekker, A., Hofmann, A., Owens, J.D., Lyons, T.W., 2012. Sulfur record of rising and falling
742 marine oxygen and sulfate levels during the Lomagundi event. *Proceedings of the National Academy of*
743 *Sciences* 109, 18300-18305.

744 Porter, S.J., Selby, D., Cameron, V., 2014. Characterising the nickel isotopic composition of organic-rich
745 marine sediments. *Chemical Geology* 387, 12-21.

746 Powell, W., 2003. Greenschist-facies metamorphism of the Burgess Shale and its implications for models of
747 fossil formation and preservation. *Canadian Journal of Earth Sciences* 40, 13-25.

748 Quirico, E., Montagnac, G., Rouzaud, J.-N., Bonal, L., Bourot-Denise, M., Duber, S., Reynard, B., 2009.
749 Precursor and metamorphic condition effects on Raman spectra of poorly ordered carbonaceous matter in
750 chondrites and coals. *Earth and Planetary Science Letters* 287, 185-193.

751 Reynaud, J.-Y., Trentesaux, A., El Albani, A., Aubineau, J., Ngombi-Pemba, L., Guiyeligou, G., Bouton, P.,
752 Gauthier-Lafaye, F., Weber, F., 2018. Depositional setting of the 2.1 Ga Francevillian macrobiota (Gabon):
753 Rapid mud settling in a shallow basin swept by high-density sand flows. *Sedimentology* 65, 670-701.

754 Robbins, L., Lalonde, S., Saito, M.A., Planavsky, N., Mloszewska, A., Pecoits, E., Scott, C., Dupont, C., Kappler,
755 A., Konhauser, K., 2013. Authigenic iron oxide proxies for marine zinc over geological time and implications
756 for eukaryotic metallome evolution. *Geobiology* 11, 295-306.

757 Rosing, M.T., 1999. ¹³C-depleted carbon microparticles in > 3700-Ma sea-floor sedimentary rocks from West
758 Greenland. *Science* 283, 674-676.

759 Samanta, M., Ellwood, M.J., Strzepek, R.F., 2018. Zinc isotope fractionation by *Emiliana huxleyi* cultured
760 across a range of free zinc ion concentrations. *Limnology and Oceanography* 63, 660-671.

761 Schulz, H.N., Jørgensen, B.B., 2001. Big bacteria. *Annual Reviews in Microbiology* 55, 105-137.

762 Scott, C., Planavsky, N.J., Dupont, C.L., Kendall, B., Gill, B.C., Robbins, L.J., Husband, K.F., Arnold, G.L., Wing,
763 B.A., Poulton, S.W., 2013. Bioavailability of zinc in marine systems through time. *Nature Geoscience* 6, 125-
764 128.

765 Sforza, M.-C., Van Zuilen, M., Philippot, P., 2014. Structural characterization by Raman hyperspectral
766 mapping of organic carbon in the 3.46 billion-year-old Apex chert, Western Australia. *Geochimica et*
767 *Cosmochimica Acta* 124, 18-33.

768 Sforza, M.C., Loron, C.C., Demoulin, C.F., François, C., Cornet, Y., Lara, Y.J., Grolimund, D., Ferreira Sanchez,
769 D., Medjoubi, K., Somogyi, A., 2022. Intracellular bound chlorophyll residues identify 1 Gyr-old fossils as
770 eukaryotic algae. *Nature communications* 13, 1-8.

771 Shen, Y., Canfield, D.E., Knoll, A.H., 2002. Middle Proterozoic ocean chemistry: evidence from the McArthur
772 Basin, northern Australia. *American Journal of Science* 302, 81-109.

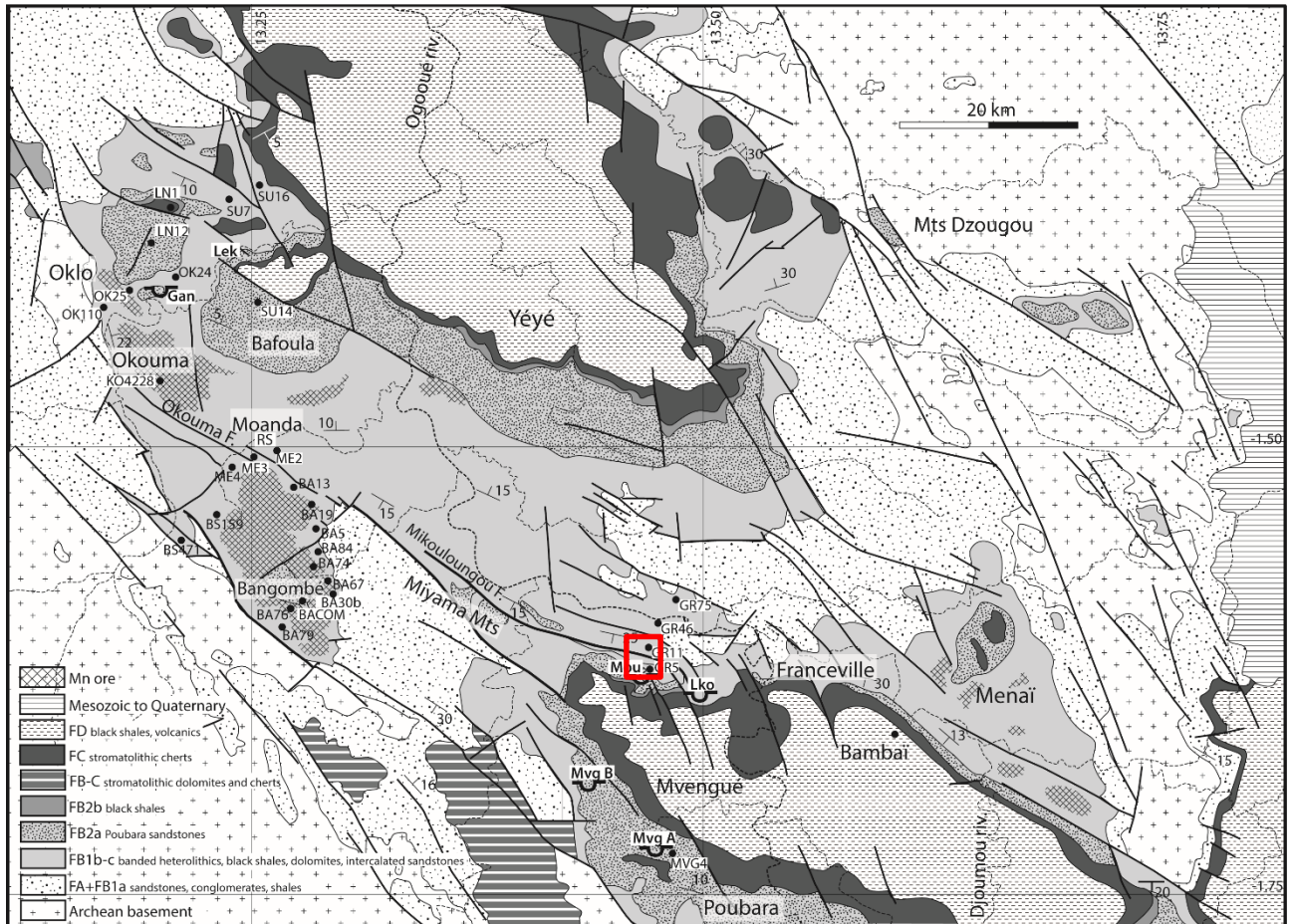
773 Solé, V.A., Papillon, E., Cotte, M., Walter, P., Susini, J., 2007. A multiplatform code for the analysis of energy-
774 dispersive X-ray fluorescence spectra. *Spectrochimica Acta Part B: Atomic Spectroscopy* 62, 63-68.

775 Somogyi, A., Medjoubi, K., Baranton, G., Le Roux, V., Ribbens, M., Polack, F., Philippot, P., Samama, J.-P.,
776 2015. Optical design and multi-length-scale scanning spectro-microscopy possibilities at the Nanoscopium
777 beamline of Synchrotron Soleil. *Journal of synchrotron radiation* 22, 1118-1129.

778 Tashiro, T., Ishida, A., Hori, M., Igisu, M., Koike, M., Méjean, P., Takahata, N., Sano, Y., Komiya, T., 2017. Early
779 trace of life from 3.95 Ga sedimentary rocks in Labrador, Canada. *Nature* 549, 516-518.
780 Thibon, F., Blichert-Toft, J., Tsikos, H., Foden, J., Albalat, E., Albarede, F., 2019. Dynamics of oceanic iron prior
781 to the Great Oxygenation Event. *Earth and Planetary Science Letters* 506, 360-370.
782 Tufail, A., Li, H., Naeem, A., Li, T., 2018. Leaf cell membrane stability-based mechanisms of zinc nutrition in
783 mitigating salinity stress in rice. *Plant Biology* 20, 338-345.
784 Twining, B.S., Baines, S.B., 2013. The trace metal composition of marine phytoplankton. *Annual review of*
785 *marine science* 5, 191-215.
786 Velde, B., Vasseur, G., 1992. Estimation of the diagenetic smectite to illite transformation in time-
787 temperature space. *American Mineralogist* 77, 967-976.
788 Wacey, D., 2009. *Early life on earth: a practical guide*. Springer Science & Business Media.
789 Weber, T., John, S., Tagliabue, A., DeVries, T., 2018. Biological uptake and reversible scavenging of zinc in the
790 global ocean. *Science* 361, 72-76.
791 Zhou, L., Kyte, F.T., 1992. Sedimentation history of the South Pacific pelagic clay province over the last 85
792 million years inferred from the geochemistry of Deep Sea Drilling Project Hole 596. *Paleoceanography* 7, 441-
793 465.

794

795



797 **Figure 1.** Geological map of the Franceville Basin. The studied outcrops are located in the Moulende
 798 quarry (red square). Structural framework and unit contours modified from Weber (1968) and
 799 Gauthier-Lafaye (1986).

800

801

802

803

804

805

806

807

808

809

810

811

812

813

814

815

816

817



818

819

820

821

822

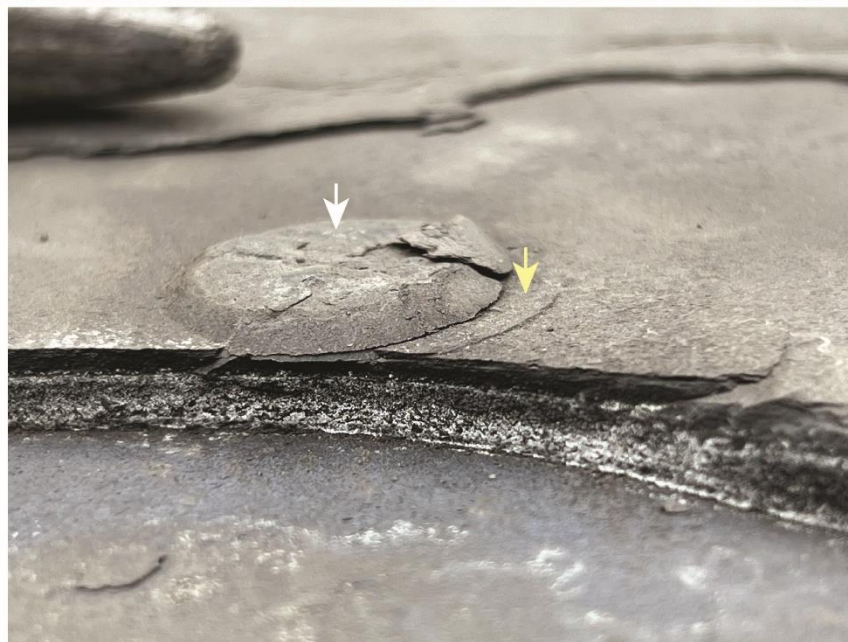
823

824

825

826

827



828 **Figure 2: (Top)** View of the outcrop: the 5 m-thick finely horizontally laminated black shales are
829 interbedded with thin, silty sandstone layers hosting the LF (black arrow), which are homogeneously
830 distributed throughout the section. **(Bottom)** The white arrow shows the body of an LF specimen,
831 while the yellow arrow points to its brim.

832

833



834

835 **Figure 3.** Plate of 24 photographs of circular forms (LF) embedded in their black shale host rock
 836 (from subunit FB2b) arranged in a (row × column) array. Scale bars represent 1 cm. The morphology
 837 is lenticular, occasionally segmented by radial structures (e.g., 1 ×2, 1×3, 3×1, 4×1), and the outline
 838 is circular. A brim is present in some of the specimens (e.g., 1×1, 1×2, 1×4, 2×2, 3×2). Other samples
 839 miss the brim (e.g., 5×3, 5×4, 6×1, 6×3). This dichotomy may represent a contrast between the
 840 bottom and the top of the organism or be a preservation artefact. The dome part is filled with
 841 organic-rich clay.

842
843
844
845
846
847
848
849
850
851
852
853
854
855
856
857
858
859
860
861
862
863
864
865
866
867
868
869
870
871
872
873
874
875
876
877
878
879
880
881
882
883
884

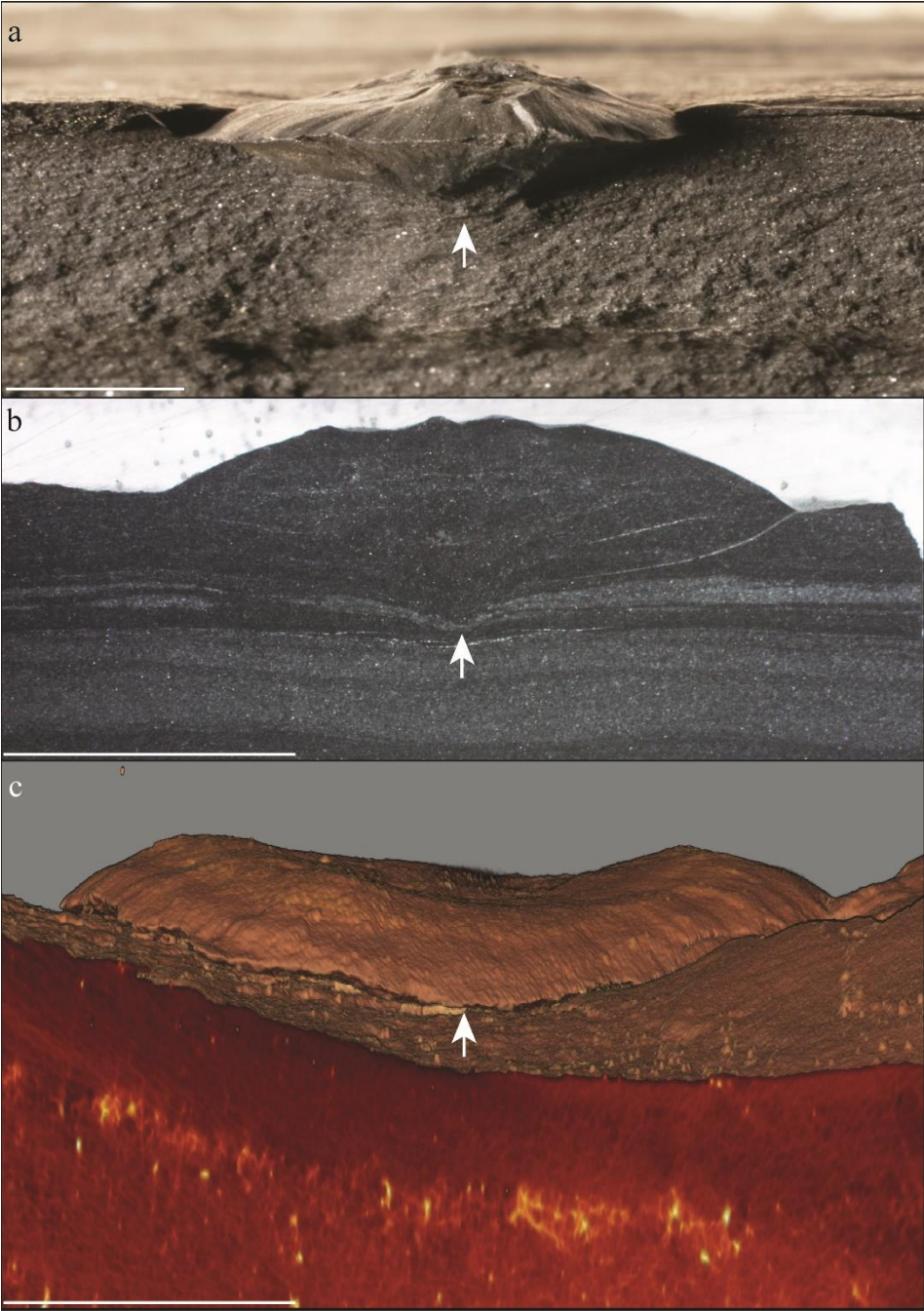
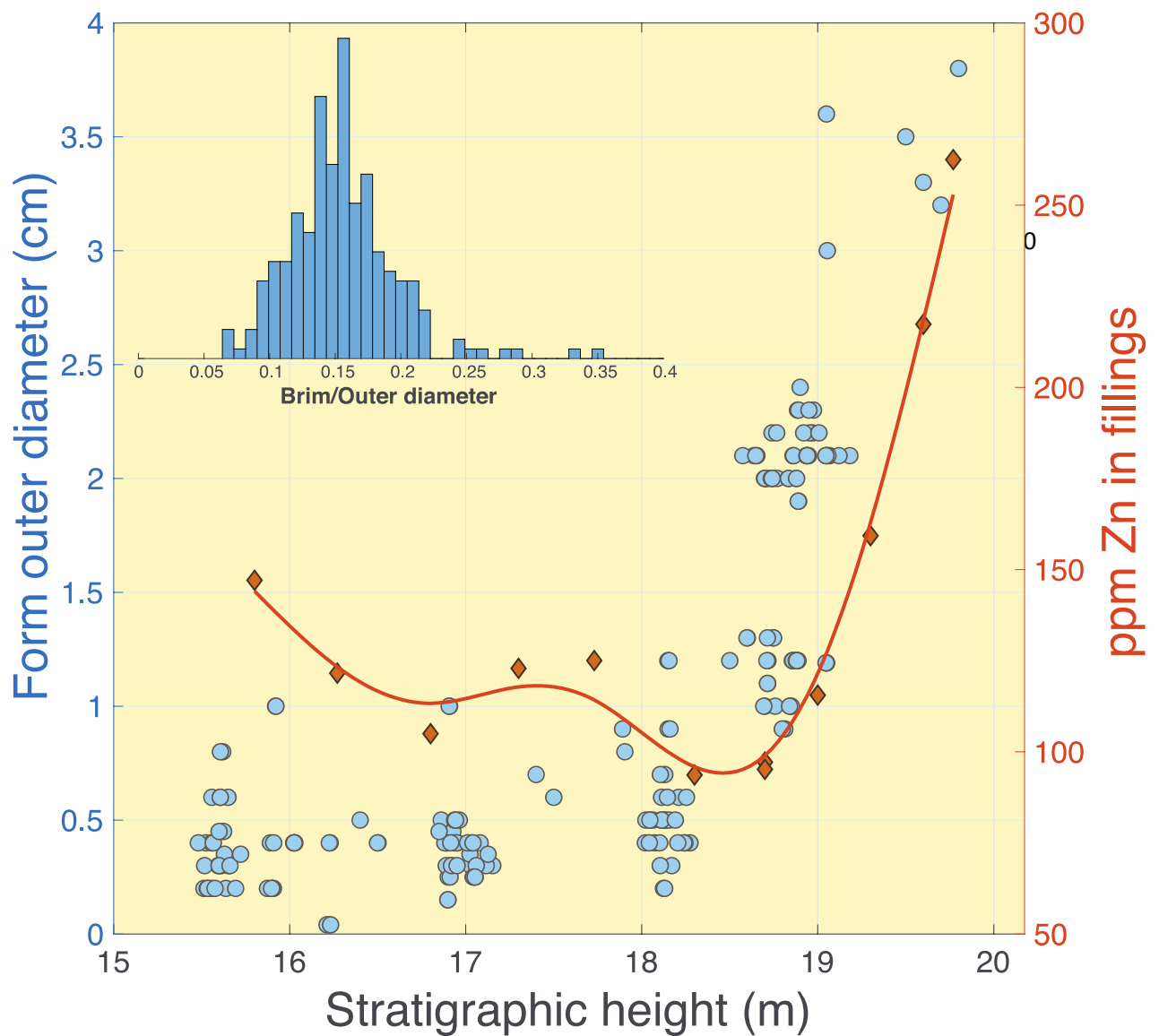


Figure 4. (a) Biconvex LF specimen surrounded by its host rock. White arrows show the upper and lower apex, respectively. Scale bars are 1 cm. **(b,c)** Two cross-sections showing the relationship between an LF specimen and its underlying sediment. **(b)**: Reflected-light microscopic view. **(c)** Three-dimensional color X-ray microtomography. In both cases, the LF is clearly observed to deflect the underlying laminae (white arrows), which attests that the LF are syndepositional features and not secondary concretions. White scale bar is 1cm.

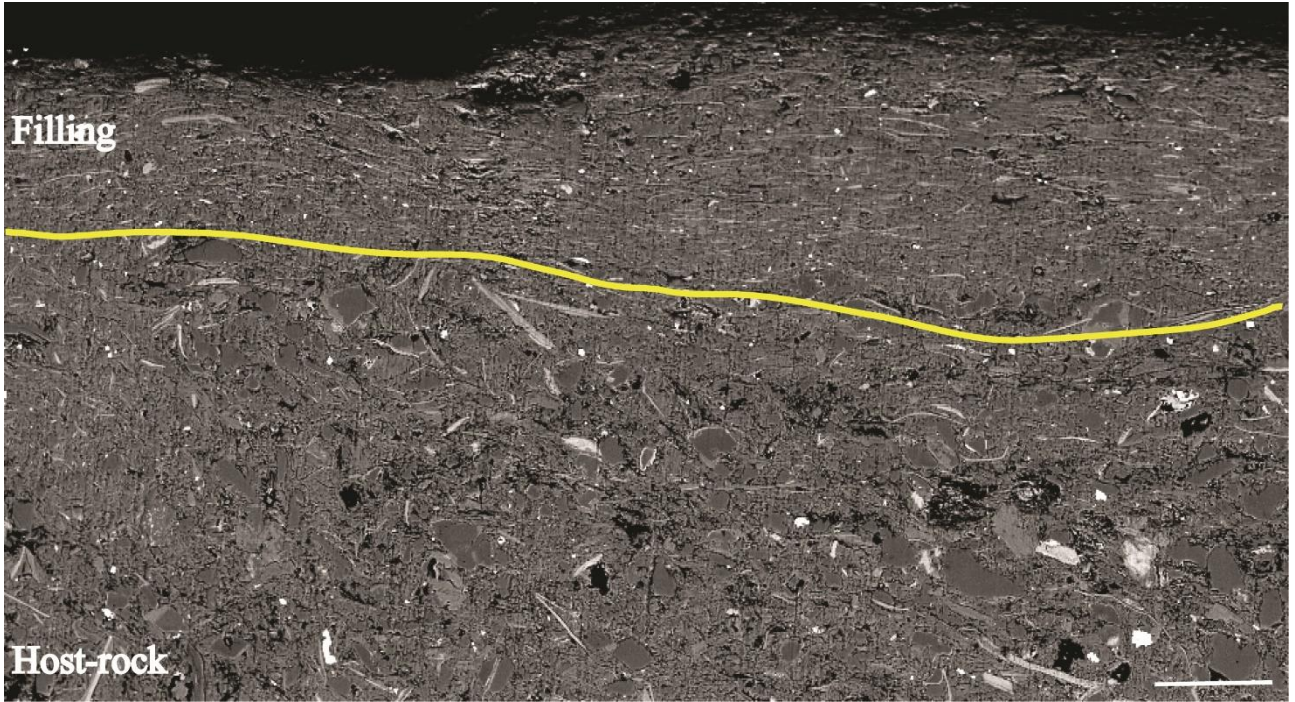
885
886
887



891
892
893
894
895

896 **Figure 5.** Lenticular form diameters (in blue) and Zn contents of their fillings (in red) vs stratigraphic
897 height. Jitter has been applied to the x-axis for better readability. The red curve is a fit of the filling
898 data with a smoothing spline. The sharp increase of both parameters starting at 18.5 m indicates
899 that a sudden increase in nutrient supply contributed to the ten-fold increase in organism size. Inset:
900 Histogram of the brim/external diameter ratio, which shows that the geometric characteristics of
901 the LF remain in constant proportion, a feature indicative of a biological origin.

902



903

904 **Figure 6.** Scanning electron microscopy-back-scattered electron imaging (SEM-BSE) coupled to
905 energy-dispersive X-ray spectrometry (EDX) showing contrast in textural and mineralogical
906 compositions within the LF comparing to the host rock. The yellow line traces the contact between
907 the LF specimen and its host rock. It shows very clearly to the naked eye that the grain size of quartz,
908 micas, and chlorite are coarser and more randomly distributed in the host rock than in the LF
909 specimen. White scale bar is 1 mm.

910

911

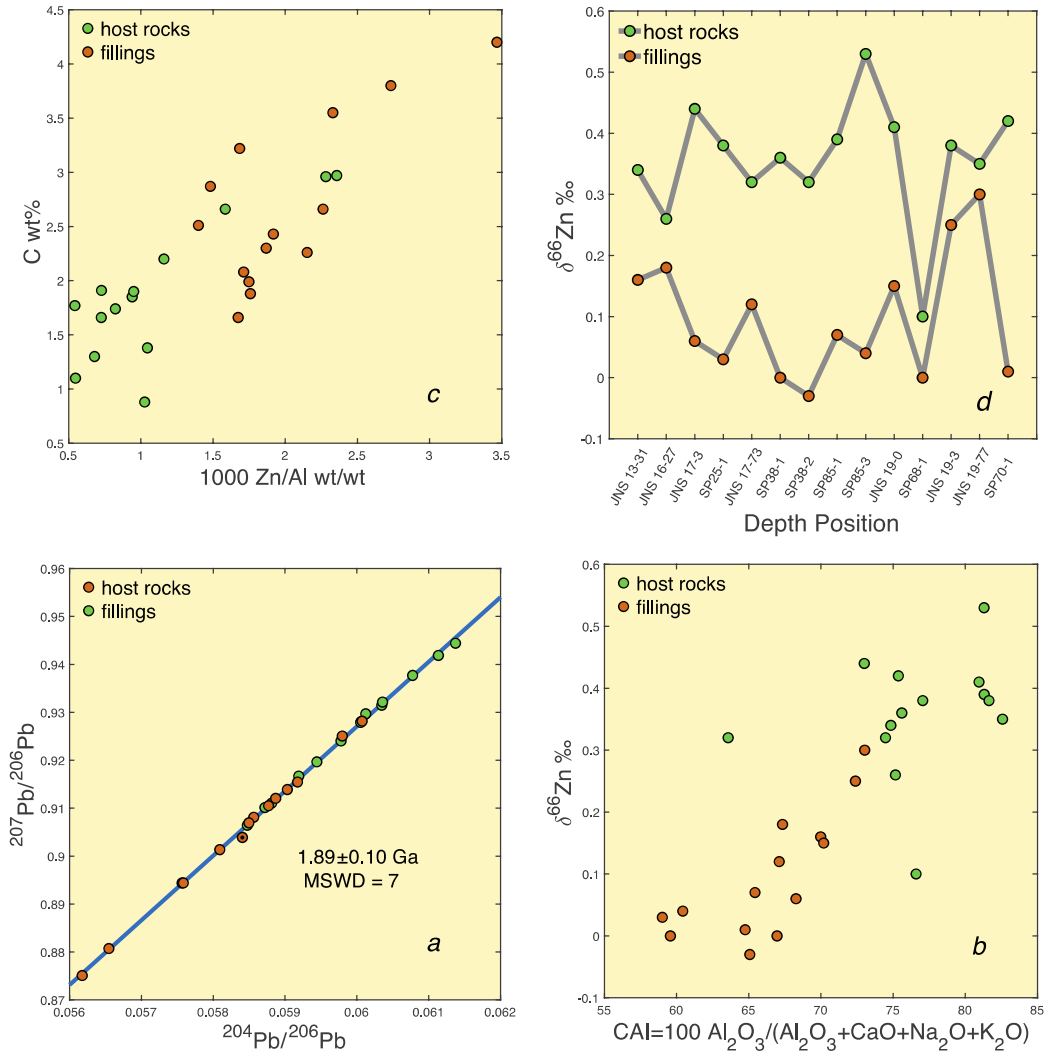
912

913

914

915

916



917
918

919 **Figure 7.** Geochemistry of the host rock of the LF and their fillings. **(a)** The Pb-Pb linear array (inverse
920 isochron) shows that if the U-Pb chronometer has been reset, it could only have been shortly after
921 sedimentation. The sample with a dotted symbol has been left out of the calculations. The error bar
922 includes correction for an MSWD value of 7 and is identical at the same confidence level to the
923 errors calculated by Monte Carlo and bootstrapping. The age is indistinguishable from literature
924 dates (Bonhomme et al., 1982; Bros et al., 1992). **(b)** Relationship between $\delta^{66}\text{Zn}$ and the Chemical
925 Index Alteration (CIA) (Nesbitt and Young, 1982). The host rock is dominated by residual material
926 from thoroughly lixiviated soils, whereas the LF fillings contain large fractions of fine-grained
927 material (clays) eroded from the continental surface. **(c)** Correlation between the organic carbon
928 contents of the host rock and the fillings and Zn/Al ratios. The main Zn carrier is clearly associated
929 with the organic component. **(d)** Comparison between the $\delta^{66}\text{Zn}$ values of the host rock and the
930 corresponding LF fillings. The $\delta^{66}\text{Zn}$ values of the host rock fall within the lithogenic range
931 ($0.28 \pm 0.13\%$ (Moynier et al., 2017)), whereas the fillings are characterized by significantly lower
932 $\delta^{66}\text{Zn}$ indicative of organic carbon sediments (Little et al., 2016). Typical error bars are 0.05‰.

933
934
935
936
937
938
939
940
941
942
943
944
945
946
947
948
949
950
951
952
953
954
955
956
957
958
959

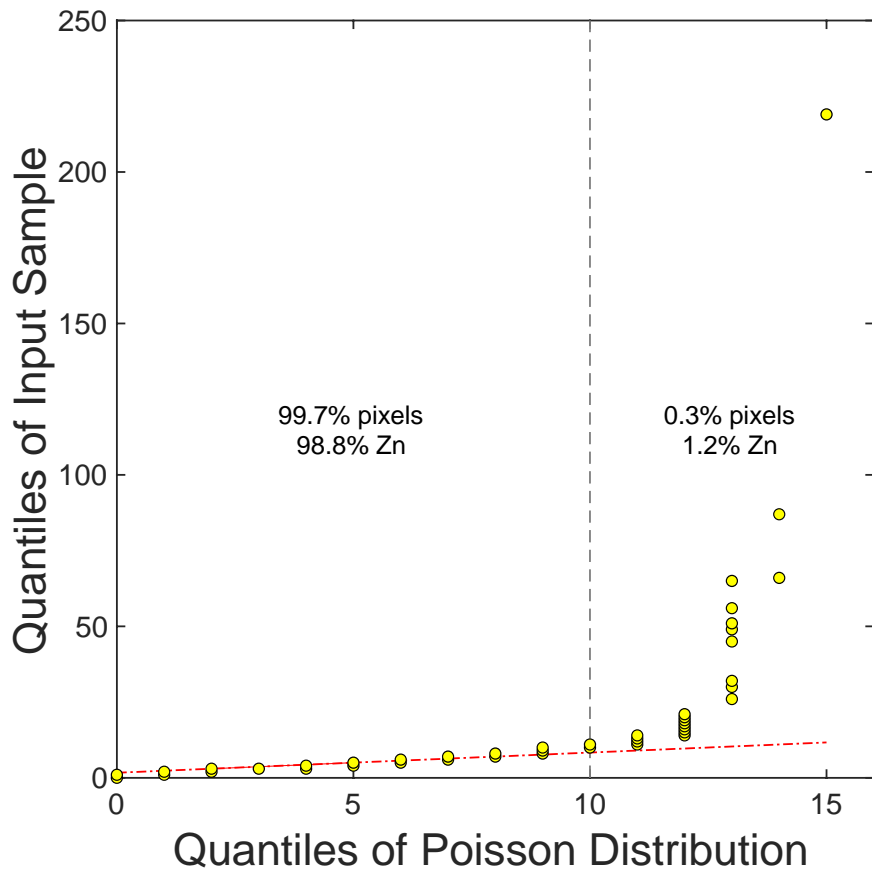


Figure 8: Quantile-quantile plot comparing, as an example, the observed frequency of the Zn intensity (counts per 10 ms per pixel) measured in the fillings by SR-XRF (shown in Fig. 7a) with the frequencies expected from a Poisson (random) distribution. The 1:1 straight-line (in stippled red) shows the perfect correspondence for low-counts pixels, which are the overwhelming majority. The array deviates from linearity at ~ 10 cps. Only 0.3 % of the pixels are outliers (>10 cp10ms) with respect to a Poisson distribution and they account for 1.2% of the total Zn concentration of the measured region. The bulk of the Zn inventory, and in particular Zn excesses, therefore should be associated with the carbon-rich background matrix and not with disseminated sulfide crystals. We found Poisson distributions with similar (Zn outlier)/(total Zn) ratios for all the measured regions.

960 **Table 1.** Mineralogical and geochemical contrasts between host rock and LF fillings. Parameter p
 961 measures the probability that the LF and their host rock belong to the same population (t-test). The
 962 standard asterisk scale is *** for $p < 0.001$, ** for $p < 0.01$, and * for $p < 0.05$.

Host rock	LF fillings	p
40% clay minerals	70% clay minerals	n/a
av. diameter of quartz grains 50 μm	av. diameter of quartz grains 25 μm	n/a
C=0.16 \pm 0.05 mol/100g	C=0.22 \pm 0.06 mol/100g	*
High Si, K, Zr, Hf High CAI	High Na, Ca, Er-Lu High Na/K, Lu/Hf	***
av. [Zn]=94 \pm 40 ppm	av. [Zn]=175 \pm 54 ppm	***
av. $\delta^{66}\text{Zn}$ =0.36 \pm 0.10‰	av. $\delta^{66}\text{Zn}$ =0.10 \pm 0.10‰	***
av. $^{206}\text{Pb}/^{204}\text{Pb}$ =16.70 \pm 0.25	av. $^{206}\text{Pb}/^{204}\text{Pb}$ =17.14 \pm 0.33	**

963

964

965

Supplementary Table S1. Zn and Pb isotope compositions of the lenticular forms and their host rocks

	$\delta^{66}\text{Zn} \text{‰}^a$	$^{206}\text{Pb}/^{204}\text{Pb}$	$\pm 2s$	$^{207}\text{Pb}/^{204}\text{Pb}$	$\pm 2s$	$^{208}\text{Pb}/^{204}\text{Pb}$	$\pm 2s$
Host rocks							
JNS 13,31	0.34	16.8229	6	15.4712	8	40.9248	25
JNS 16,27	0.26	16.6325	7	15.4628	7	45.4806	24
JNS 17,3	0.44	17.0301	9	15.5003	9	47.9881	31
SP25-1	0.38	16.5712	6	15.4355	7	42.9549	22
JNS 17,73	0.32	16.6512	6	15.4529	7	45.2254	22
SP38-1	0.36	16.7282	9	15.4573	11	40.4249	37
SP38-2	0.32	16.3574	8	15.4062	11	39.1924	33
SP85-1	0.39	16.6520	5	15.4514	5	40.9423	14
SP85-3	0.53	16.2938	5	15.3882	7	41.0597	21
JNS 19,0	0.41	17.0031	8	15.4908	8	47.9608	26
SP68-1	0.10	16.8948	6	15.4873	7	41.2919	23
JNS 19,3	0.38	16.4538	10	15.4284	12	40.9575	41
JNS 19,77	0.35	17.1014	7	15.5010	10	45.0732	20
SP70-1	0.42	16.5680	6	15.4434	5	43.7276	17
Lenticular forms							
JNS 13-31	0.16	16.9865	7	15.4925	6	40.5764	19
JNS 16-27	0.18	16.7234	8	15.4700	6	44.5041	21
JNS 17-3	0.06	17.3712	9	15.5368	9	49.1236	28
SP25-1	0.03	17.8013	8	15.5778	7	48.4227	53
JNS 17-73	0.12	17.2144	10	15.5159	10	45.9137	32
SP38-1	0.00	16.9399	6	15.4811	6	40.7712	18
SP38-2	-0.03	16.8993	6	15.4701	7	40.7763	22
SP85-1	0.07	17.0152	8	15.4925	7	41.3270	20
SP85-3	0.04	17.1217	10	15.4762	10	41.6602	34
JNS 19-0	0.15	17.6843	8	15.5746	9	45.4911	26
SP68-1	0.00	17.0752	9	15.5066	8	41.7341	26
JNS 19-3	0.25	16.6464	8	15.4506	8	41.2924	22
JNS 19-77	0.30	17.0952	9	15.5042	9	44.4140	30
SP70-1	0.01	17.3660	6	15.5327	4	44.3411	18

^a precision $\pm 0.05\text{‰}$ ^b probability (t-test) 7.3E-07 1.2E-03 2.3E-03 6.9E-01

Table S2: Major and trace elements of the fillings and the host rocks of the circular forms

	unit	Host rocks														ρ^a
		JNS 3,31	JNS 16,27	JNS 7,3	SP 25-1	JNS 17,73	SP 38-1	SP 38-2	SP 85-1	SP 85-3	JNS 19,0	SP 68-1	JNS 19,3	JNS 19,77	SP 70-1	
height	m	13.31	16.27	17.3	16.8	17.73	18.3	18.3	18.7	18.7	19	19.6	19.3	19.77	15.8	
SiO ₂	%	58.30	57.81	58.09	57.16	54.74	57.89	57.56	61.27	61.45	62.88	58.21	61.85	58.93	56.76	1.4E-07
Al ₂ O ₃	%	18.86	18.60	17.07	20.79	12.06	18.85	17.86	19.06	18.81	18.65	18.30	15.14	16.69	18.68	3.7E-01
Fe ₂ O ₃	%	2.36	2.20	2.81	2.46	6.50	2.27	2.32	3.71	4.47	3.44	2.51	3.81	3.69	2.28	1.5E-01
MnO	%	0.24	0.26	0.44	0.28	0.74	0.26	0.27	0.15	0.10	0.07	0.39	0.23	0.49	0.32	6.0E-01
MgO	%	2.86	2.74	3.06	2.71	5.55	2.74	2.74	1.97	1.96	1.96	2.63	3.02	3.43	2.79	3.4E-01
CaO	%	2.18	2.07	2.67	1.52	5.21	1.95	2.14	0.32	0.34	0.37	1.60	0.27	0.23	2.02	2.9E-05
Na ₂ O	%	0.38	0.35	0.33	0.41	0.23	0.40	0.39	0.36	0.36	0.39	0.38	0.30	0.34	0.39	1.2E-06
K ₂ O	%	3.79	3.73	3.32	4.27	1.47	3.73	3.60	3.71	3.64	3.63	3.62	2.83	2.95	3.71	7.9E-02
TiO ₂	%	0.40	0.39	0.39	0.46	0.32	0.41	0.36	0.40	0.39	0.41	0.39	0.42	0.33	0.40	8.4E-03
P ₂ O ₅	%	0.14	0.16	0.13	0.12	0.12	0.13	0.15	0.20	0.17	0.17	0.16	0.20	0.05	0.15	4.0E-01
CAI		74.84	75.16	73.00	77.05	63.57	75.60	74.47	81.31	81.30	80.95	76.59	81.64	82.58	75.36	9.5E-06
As	ppm	0.8	0.8	0.8	1.25	7.0	0.82	1.17	0.75	1.33	10.9	<L.D.	1.4	0.4	0.79	5.9E-01
Ba	ppm	1448	1482	1294	1705	651	1466	1404	1434	1424	1505	1445	1137	1132	1528	2.2E-01
Be	ppm	1.5	1.6	1.3	1.91		1.75	1.68	1.61	1.85	1.5	1.58	1.7	1.3	1.71	2.7E-01
Cd	ppm	0.3	0.7	0.4	0.11	0.4		0.07	0.04	0.05	0.3	0.54	0.1	0.2	0.03	
Co	ppm	5.3	5.1	4.2	6.21	20.1	4.59	5.73	5.76	6.38	8.9	4.86	6.7	5.3	6.47	3.2E-01
Cr	ppm	33.2	33.8	36.3	55.5	40.6	49.9	46.7	51.3	49.9	54.8	49.7	41.7	37.0	49.5	5.1E-02
Cs	ppm	11.0	10.7	8.5	13.8	5.5	12.1	11.3	11.1	11.1	11.1	11.2	9.0	8.0	11.5	4.3E-02
Cu	ppm	57.0	51.9	58.0	20.7	34.6	62.1	64.4	24.8	16.3	56.6	95.5	56.1	40.1	64.0	1.9E-01
Ga	ppm	23.0	23.9	21.3	27.7	17.1	24.5	22.9	23.5	23.8	23.9	23.5	20.0	20.6	24.4	3.9E-01
Ge	ppm	2.5	2.4	2.4	2.66	2.3	2.37	2.22	2.35	2.67	2.1	2.24	2.1	2.0	2.41	8.9E-01
Hf	ppm	4.6	5.0	5.1	2.29	6.8	4.24	4.93	4.58	4.33	5.6	4.78	5.6	3.5	5.04	1.1E-07
Mo	ppm	0.3	0.3	0.3	1.05	0.8	1.04	1.15	1.28	1.39	0.8	1.02	0.3	0.3	1.15	4.8E-03
Nb	ppm	5.3	5.5	5.6	6.14	4.6	5.72	5.28	5.66	5.55	5.9	5.75	5.6	4.1	5.82	3.6E-03
Ni	ppm	33.5	33.9	42.6	55.1	83.2	42.8	43.6	66.7	82.7	60.7	47.2	52.1	48.9	45.8	2.2E-01
Pb	ppm	18.1	12.3	15.0	16.9	13.4	6.14	9.50	5.95	9.38	10.8	3.89	8.4	5.1	6.23	6.5E-01
Rb	ppm	123.8	126.1	108.4	150	53.9	132	122	125	125	125.3	127	105.3	95.2	132	1.6E-01
Sb	ppm	0.3	0.3	0.3	0.37	0.8	0.21	0.28	0.23	0.38	0.5	0.17	0.3	0.2	0.29	9.2E-01
Sc	ppm	8.4	7.9	7.4	9.19		8.53	8.21	8.55	8.73		8.67	7.8	9.3	9.10	7.8E-01
Sn	ppm	4.1	1.6	1.9	1.08	1.3	1.18	2.02	0.82	0.88	1.3	0.91	1.2	0.8	0.87	3.7E-02
Sr	ppm	84.0	85.9	91.6	90.6	70.0	93.7	88.2	83.0	78.5	86.3	88.1	94.2	74.2	90.2	2.7E-05
Ta	ppm	0.5	0.5	0.5	0.50	0.4	0.47	0.47	0.50	0.48	0.5	0.52	0.5	0.4	0.50	2.3E-03
Th	ppm	12.8	13.5	13.5	15.1	10.8	14.2	13.0	13.7	13.8	14.4	15.3	16.0	10.0	14.7	2.6E-01
U	ppm	1.2	1.2	1.2	1.20	1.1	1.17	1.17	1.17	1.16	1.2	1.15	1.3	0.8	1.24	7.9E-03
V	ppm	50.7	50.0	49.5	59.3	32.4	52.0	47.4	46.5	48.3	53.0	46.9	38.7	43.0	52.0	6.2E-01
W	ppm	1.6	1.7	1.8	1.66	1.0	1.29	1.95	1.97	1.89	1.7	1.62	2.1	1.3	1.79	8.4E-02
Y	ppm	14.3	13.6	12.8	11.5	13.8	13.1	13.1	16.3	19.1	14.3	12.9	13.9	10.2	14.4	6.1E-02
Zn	ppm	54.2	53.9	65.6	91.4	150.5	64.1	190	93.1	139	93.9	70.5	82.3	102.4	59.3	3.1E-04
Zr	ppm	179.9	192.2	197.0	81.0	265.4	163	189	172	164	220.0	183	210.1	134.8	190	1.6E-07
La	ppm	41.9	40.2	39.4	41.0	23.5	43.4	40.8	45.1	40.0	43.4	44.4	52.8	30.0	41.1	8.3E-01
Ce	ppm	76.9	74.2	73.9	74.9	44.3	79.5	75.1	83.2	74.4	80.4	81.6	97.1	57.0	76.5	9.3E-01
Pr	ppm	8.2	8.0	8.0	8.09	4.9	8.58	8.10	8.90	8.08	8.7	8.85	10.3	6.2	8.26	8.2E-01
Nd	ppm	28.5	28.0	28.1	28.0	18.2	29.9	28.4	30.7	28.3	30.6	30.4	35.5	22.2	28.8	9.6E-01
Sm	ppm	4.5	4.6	4.5	4.35	3.2	4.70	4.60	4.79	4.29	4.9	4.72	5.4	3.6	4.66	3.8E-01
Eu	ppm	1.0	1.0	1.0	0.984	0.8	1.04	1.00	1.03	1.01	1.1	1.02	1.2	0.8	1.06	3.0E-01
Gd	ppm	3.2	3.4	3.2	3.20	2.6	3.38	3.18	3.48	3.49	3.5	3.27	3.7	2.6	3.40	2.7E-01
Tb	ppm	0.4	0.4	0.4	0.406	0.4	0.426	0.418	0.445	0.467	0.5	0.406	0.5	0.3	0.440	8.4E-02
Dy	ppm	2.3	2.3	2.2	2.04	2.1	2.29	2.23	2.47	2.63	2.4	2.17	2.5	1.8	2.36	1.2E-02
Ho	ppm	0.5	0.4	0.4	0.379	0.4	0.439	0.439	0.495	0.532	0.4	0.427	0.5	0.3	0.471	5.0E-03
Er	ppm	1.2	1.1	1.1	0.930	1.1	1.10	1.12	1.24	1.33	1.2	1.10	1.2	0.9	1.18	2.4E-04
Tm	ppm	0.2	0.2	0.1	0.124	0.2	0.149	0.154	0.161	0.171	0.2	0.145	0.2	0.1	0.157	2.5E-06
Yb	ppm	1.1	1.0	1.0	0.790	1.1	0.964	1.00	1.01	1.09	1.1	0.989	1.1	0.7	1.05	2.4E-07
Lu	ppm	0.158	0.153	0.158	0.112	0.167	0.140	0.145	0.148	0.157	0.159	0.141	0.162	0.110	0.152	3.6E-07

Table S2: continued

		Fillings													
	unit	NS 13-3	NS 16-2	NS 17-3	SP25-1	NS 17-7	SP38-1	SP38-2	SP85-1	SP85-3	NS 19-4	SP68-1	NS 19-3	NS 19-7	SP70-1
SiO ₂	%	52.03	54.24	52.70	47.74	52.00	49.79	53.89	51.89	49.36	53.30	53.02	55.57	55.35	49.79
Al ₂ O ₃	%	18.86	18.39	18.48	17.07	18.60	16.15	17.32	19.35	17.80	18.95	19.05	19.23	19.87	19.30
Fe ₂ O ₃	%	3.37	2.07	2.83	1.54	2.47	2.14	2.51	2.43	2.31	2.68	2.02	3.87	4.06	2.24
MnO	%	0.30	0.16	0.40	0.21	0.77	0.23	0.27	0.25	0.33	0.77	0.38	0.24	0.15	0.29
MgO	%	2.97	2.63	3.10	2.23	2.74	2.43	2.61	2.59	2.72	2.86	2.68	2.54	1.99	2.74
CaO	%	3.61	3.73	3.95	5.99	3.80	5.62	4.47	4.63	5.93	3.46	3.99	2.51	2.08	4.84
Na ₂ O	%	0.85	1.42	1.03	2.21	1.42	1.97	1.25	1.43	1.85	0.82	1.33	1.17	1.19	1.57
K ₂ O	%	3.63	3.77	3.61	3.67	3.90	3.38	3.57	4.17	3.88	3.78	4.08	3.67	4.07	4.10
TiO ₂	%	0.36	0.33	0.33	0.32	0.32	0.31	0.32	0.41	0.36	0.37	0.37	0.39	0.39	0.40
P ₂ O ₅	%	0.32	0.14	0.14	0.14	0.14	0.19	0.14	0.17	0.16	0.11	0.15	0.12	0.18	0.16
CAI		69.98	67.34	68.27	59.01	67.11	59.57	65.07	65.43	60.43	70.19	66.96	72.39	73.03	64.75
As	ppm	3.772	0.551	<L.D.	0.7	0.888	0.7	1.1	1.0	0.880	2.4	4.9	2.1	0.6	
Ba	ppm	1434	1433	1390	1496	1514	1264	1341	1508	1419	1496	1595	1394	1597	1551
Be	ppm	1.7	1.7	1.6	1.7	1.6	1.7	1.7	1.8	1.6	1.7	1.7	1.3	2.1	1.8
Cd	ppm	0.1		0.0	0.0	0.0		0.0	0.1	0.2	0.0	1.0	0.6	0.2	0.1
Co	ppm	13.5	3.3	4.4	5.6	5.6	5.1	5.3	6.7	6.1	8.9	7.4	17.0	32.8	3.6
Cr	ppm	46.2	46.2	46.9	48.2	48.5	49.2	46.6	60.9	47.5	50.3	50.0	53.7	54.3	51.7
Cs	ppm	7.7	12.2	11.3	12.9	12.1	11.7	11.5	13.0	12.3	12.3	12.9	11.1	13.4	12.8
Cu	ppm	175.0	61.4	62.0	86.9	54.0	86.6	78.2	22.0	27.4	111.0	21.2	54.1	39.8	40.5
Ga	ppm	24.2	23.0	23.1	22.3	24.0	20.8	21.5	24.9	23.1	24.6	24.8	24.2	25.5	25.5
Ge	ppm	2.2	2.1	2.5	1.8	2.1	2.0	2.0	2.5	2.4	2.6	2.4	2.7	2.7	2.3
Hf	ppm	3.3	2.3	2.3	1.8	2.0	2.3	2.6	1.5	1.7	2.3	1.9	2.3	2.1	1.9
Mo	ppm	1.9	1.0	0.8	1.0	1.3	1.3	0.8	1.2	1.6	1.3	1.3	1.5	1.0	1.1
Nb	ppm	5.3	4.9	4.7	4.6	4.8	4.6	4.7	5.3	4.8	5.1	5.1	5.3	5.3	5.4
Ni	ppm	81.5	39.1	49.9	71.2	48.0	48.6	46.9	58.0	51.6	58.4	50.1	82.1	137.2	41.6
Pb	ppm	14.3	5.3	4.2	4.2	5.7	5.7	3.7	10.4	11.7	6.6	20.2	18.1	9.4	6.5
Rb	ppm	120.0	127.2	122.1	128.2	130.9	115.3	117.9	135.1	124.9	133.1	139.7	121.6	139.7	138.3
Sb	ppm	0.8	0.3	0.2	0.2	0.2	0.2	0.1	0.3	0.2	0.3	0.5	0.6	0.5	0.3
Sc	ppm	9.7	7.8	8.1	8.3	7.9	7.4	7.3	7.2	7.2	8.5	8.2	9.5	11.6	7.4
Sn	ppm	5.8	1.1	1.3	5.0	1.2	2.3	1.1	2.5	5.2	4.6	2.3	1.0	1.4	2.5
Sr	ppm	85.2	105.7	106.7	132.1	103.9	113.4	101.0	103.0	109.2	102.6	101.4	93.1	103.7	106.7
Ta	ppm	0.5	0.4	0.4	0.4	0.4	0.5	0.4	0.4	0.4	0.4	0.4	0.5	0.5	0.4
Th	ppm	10.5	13.9	13.5	14.5	13.9	14.0	13.3	11.3	10.6	13.0	14.1	13.4	12.7	12.9
U	ppm	1.0	1.0	0.9	1.1	1.1	1.0	0.9	1.0	1.1	0.9	1.1	1.4	1.0	1.1
V	ppm	51.2	47.8	45.4	51.9	48.7	44.5	46.6	52.8	48.7	46.0	51.9	48.9	49.8	52.0
W	ppm	1.6	1.2	1.4	2.7	1.7	6.4	1.8	4.0	3.7	1.7	1.8	1.6	2.0	4.0
Y	ppm	14.5	10.4	10.0	10.6	10.0	9.5	10.1	10.0	10.2	11.3	9.6	11.4	22.5	10.6
Zn	ppm	205.4	144.8	151.1	180.5	166.8	126.4	119.9	126.5	146.4	151.7	243.3	193.5	321.9	168.6
Zr	ppm	128.6	82.8	84.7	66.9	73.6	83.6	93.4	54.2	60.2	84.8	67.4	87.2	78.2	68.9
La	ppm	33.2	39.7	42.1	46.5	39.7	43.2	41.1	36.4	33.9	43.5	37.2	34.6	49.1	36.6
Ce	ppm	62.4	73.7	78.1	88.9	73.4	79.2	75.4	69.9	64.3	80.3	68.0	64.3	91.3	67.8
Pr	ppm	6.9	8.0	8.4	9.1	7.9	8.5	8.1	7.3	6.8	8.6	7.4	7.1	9.9	7.3
Nd	ppm	25.3	27.9	29.4	31.3	28.0	29.7	28.0	25.2	24.2	30.4	25.6	25.3	36.0	26.0
Sm	ppm	4.25	4.23	4.35	4.42	4.21	4.31	4.15	4.18	3.97	4.54	3.94	4.05	5.61	4.17
Eu	ppm	1.02	0.92	0.94	0.92	0.94	0.92	0.87	0.96	0.96	1.00	0.90	0.93	1.33	0.96
Gd	ppm	3.24	2.90	2.92	3.01	2.89	2.85	2.80	3.12	3.11	3.04	2.79	2.94	4.51	3.13
Tb	ppm	0.42	0.36	0.35	0.37	0.36	0.35	0.34	0.37	0.38	0.37	0.34	0.38	0.58	0.39
Dy	ppm	2.32	1.83	1.77	1.84	1.83	1.83	1.82	1.94	1.91	1.93	1.73	1.95	2.97	2.07
Ho	ppm	0.44	0.35	0.34	0.34	0.34	0.33	0.34	0.34	0.34	0.35	0.32	0.36	0.57	0.36
Er	ppm	1.10	0.85	0.85	0.83	0.84	0.80	0.84	0.80	0.79	0.88	0.77	0.87	1.35	0.87
Tm	ppm	0.14	0.11	0.11	0.11	0.11	0.10	0.11	0.10	0.10	0.11	0.10	0.11	0.15	0.11
Yb	ppm	0.91	0.70	0.70	0.71	0.66	0.68	0.73	0.61	0.64	0.71	0.65	0.74	0.92	0.66
Lu	ppm	0.130	0.102	0.103	0.102	0.096	0.102	0.108	0.090	0.092	0.110	0.093	0.106	0.139	0.098

Table S2: continued

		Host rocks														
	<i>unit</i>	JNS	JNS	JNS	SP	JNS	SP	SP	SP	SP	JNS	SP	JNS	JNS	SP	<i>p</i> ^a
		3,31	16,27	7,3	25-1	17,73	38-1	38-2	85-1	85-3	19,0	68-1	19,3	19,77	70-1	
Th/U		10.364	10.867	10.955	12.551	10.009	12.075	11.16	11.722	11.903	11.924	13.331	12.121	12.097	11.818	<i>0.11</i>
Lu/Hf		0.034	0.030	0.031	0.049	0.025	0.033	0.029	0.032	0.036	0.028	0.030	0.029	0.031	0.030	<i>1.2E-06</i>
Ce/Ce ^{*b}		0.96	0.96	0.97	0.96	0.96	0.96	0.96	0.97	0.96	0.97	0.96	0.97	0.97	0.97	<i>0.18</i>
Eu/Eu ^{*b}		1.15	1.10	1.11	1.11	1.21	1.10	1.11	1.07	1.10	1.10	1.10	1.15	1.15	1.13	<i>0.95</i>
Y/Y ^{*d}		1.17	1.14	1.14	1.10	1.26	1.10	1.12	1.24	1.36	1.18	1.13	1.09	1.11	1.15	<i>0.26</i>
		Fillings														
	<i>unit</i>	JNS	JNS	JNS	SP	JNS	SP	SP	SP	SP	JNS	SP	JNS	JNS	SP	
		3,31	16,27	7,3	25-1	17,73	38-1	38-2	85-1	85-3	19,0	68-1	19,3	19,77	70-1	
Th/U		10.1	14.321	15.034	13.657	13.192	13.411	14.238	10.969	9.3088	14.506	12.685	9.9147	12.519	11.528	
Lu/Hf		0.039	0.044	0.044	0.056	0.049	0.044	0.042	0.059	0.054	0.048	0.048	0.045	0.065	0.051	
Ce/Ce [*]		0.96	0.96	0.97	1.01	0.96	0.97	0.97	1.00	0.98	0.97	0.96	0.96	0.96	0.96	
Eu/Eu [*]		1.16	1.10	1.11	1.07	1.14	1.10	1.08	1.12	1.15	1.14	1.14	1.14	1.12	1.12	
Y/Y [*]		1.22	1.10	1.09	1.13	1.07	1.03	1.09	1.03	1.06	1.16	1.09	1.15	1.46	1.03	
Zn _{xs} (Fe) ^c		128	94	85	123	110	66	28	66	74	79	187	110	209	110	
Zn _{xs} (Zr) ^c		167	122	123	105	125	94	78	97	95	116	217	159	262	147	

^a probability that the host rock and the filling belong to the same population (*t*-test). In italic, values <0.0003.

^b Ce/Ce^{*}= Ce_N/(La_N×Pr_N)^{1/2}, Eu/Eu^{*}= Eu_N/(Sm_N×Gd_N)^{1/2}, Y/Y^{*}= Y_N/(Dy_N×Ho_N)^{1/2}

where N indicates normalization to MuQ values of Kamber et al. (2005)

^c See main text for the Zn excess formula

Supplementary Table S3. C, P, and S contents of the lenticular forms and their host rocks

		C	P	C/P	S
units	sample	mol/100g	mol/100g	mol/mol	ppm
Host rocks	SP38-1	0.1594	0.0020	81	<100
	SP38-2	0.2467	0.0023	109	540
	SP85-1	0.1153	0.0030	38	380
	SP85-3	0.2219	0.0026	86	<100
	SP68-1	0.1451	0.0024	60	<100
	SP70-1	0.1080	0.0023	48	520
	SP25-1	0.1543	0.0018	85	540
	JNS 13,31	0.1472	0.0020	75	481
	JNS 16,27	0.0917	0.0023	41	<100
	JNS 17,3	0.1383	0.0018	75	<100
	JNS 17,73	0.2475	0.0017	146	<100
	JNS 19,0	0.1587	0.0024	66	<100
	JNS 19,3	0.0733			133
	JNS 19,77	0.1832			<100
Lenticular forms	SP38-1	0.1383	0.0029	48	410
	SP38-2	0.2392	0.0021	113	<100
	SP85-1	0.2093	0.0026	82	<100
	SP85-3	0.1567	0.0024	65	<100
	SP68-1	0.3168	0.0023	140	<100
	SP70-1	0.1917	0.0024	79	<100
	SP25-1	0.2219	0.0021	105	<100
	JNS 13,31	0.2955	0.0048	61	3390
	JNS 16,27	0.2683	0.0021	127	<100
	JNS 17,3	0.1658	0.0021	78	<100
	JNS 17,73	0.2023	0.0021	96	<100
	JNS 19,0	0.1733	0.0017	104	<100
	JNS 19,3	0.1886	0.0018	104	2340
	JNS 19,77	0.3503	0.0027	129	510

average and stand. dev. host rocks

76 30

average and stand. dev. infillings

95 27

probability (t -test)

0.038

0.329

0.306

Supplementary Table S4. $\delta^{13}\text{C}$ data measured on the carbon fractions of LF fillings (1) and host sediments (2).

sample	$\delta^{13}\text{C}$ (‰)
JN-21-63-1	-34.87
JN-21-63-2	-34.93
JN-21-83-1	-34.55
JN-21-83-2	-33.99
JN-21-M13-1	-34.76
JN-21-M13-2	-34.59
JN-21-68.1	-34.93
JN-21-68-2	-34.83
JN-21-M14-1	-34.02
JN-21-M14-2	-34.11

Credit author statement

Author Contributions: A.E.A. designed the research. A.E.A., F.A., J.B.T., A.S., and K.O.K. wrote the manuscript. A.E.A, E.C.F, and J.N.G did the field work. J.N.G., C.F., J.N.G., and A.E.A. prepared the samples and performed XRD analyses and models. A.M. performed X-Ray microtomography. A.E.A. analyzed morphology, A.R. analyzed carbon and sulfur concentrations. A.C.P.W. analyzed carbon isotopes. A.L. analyzed Zn and Pb isotope compositions with assistance from J.B.T. A.S carried out the synchrotron experiments and processed the data.